Department of Precision and Microsystems Engineering

Design and Experimental Testing of Energy Absorbing Mechanical Metamaterials

Pepijn Westland

Report no : 2025.038
Supervisor : F.G.J. (Freek) Broeren Phd MSc
Specialisation : MSD
Type of report : Master Thesis
Date : 18/07/2025

TU Delft Delft University of Technology

Design and Experimental Testing of Energy Absorbing Mechanical Metamaterials

MSc Thesis Report

by

Pepijn Westland

to obtain the degree of Master of Science
at the Delft University of Technology
to be defended publicly on July 31, 2025 at 14:00

Thesis committee:	
Chair:	F.G.J. (Freek) Broeren Phd MSc, TU Delft
Assessment committee:	Dr.ir. R.A.J. (Ron) van Ostayen, TU Delft
Place:	Faculty of Mechanical Engineering, Delft
Project Duration:	May, 2024 - July, 2025
Student number:	4494407

Abstract

This thesis explores the design, characterization, and experimental testing of energy absorbing mechanical metamaterials with a focus on bistable triangle structures. A comprehensive literature review categorizes existing energy absorbing metamaterials based on complexity, bistability, and energy dissipation characteristics, revealing significant research gaps in quantifying and correlating design parameters to performance metrics, particularly the energy absorption. To address these gaps, a novel, cost-effective, and repeatable dynamic impact tester was developed, inspired by the Charpy impact test but optimized for energy absorption testing. Using this dynamic tester and quasi static tests, a series of 3D-printed bistable triangular flexures were evaluated. Results highlight the influence of geometrical parameters such as flexure angle, thickness, and flexure geometry on energy dissipation. Notably, samples with a high angle demonstrated a high energy dissipation compared to low angle flexures. The findings establish foundational design guidelines and provide insights into optimizing mechanical metamaterials for applications in reusable, impact-absorbing systems.

Contents

Chapter 1

Introduction

In modern automotive design, safety is one of the most important areas of development. Modern vehicles are equipped with large crumple zones that effectively absorb energy during a collision. However, these structures deform permanently, often resulting in the vehicle being classified as a total economic loss, even after a relatively minor crash.

An emerging alternative involves the use of non-destructive, energy absorbing impact structures that can endure repeated impacts and be easily restored to their original shape. This approach has the potential to significantly reduce the environmental impact of crash structures by minimizing material waste and enabling reusability. Similar concepts could also be applied in other areas requiring impact protection, such as road infrastructure.

Mechanical metamaterials offer exciting opportunities to address these challenges. Unlike conventional materials, their unique behaviour is not solely defined by their material composition but mainly by the engineered design of their internal structure.

Despite growing interest and research in this field, a systematic understanding of how specific design parameters, affect overall energy dissipating performance remains limited. Gaining deeper insight into these relationships is essential for the further development of energy dissipating metamaterials.

This thesis addresses these gaps by exploring the design space of bistable mechanical metamaterials and experimentally evaluating their energy dissipating performance. To facilitate this, a custom designed dynamic impact tester is developed, allowing for systematic, repeatable testing of samples under controlled conditions.

The structure of this thesis is as follows:

Chapter 1: Literature Review This chapter presents a comprehensive overview of energy dissipating mechanical metamaterials. It introduces key concepts such as bistability and negative stiffness, and categorizes a wide range of designs based on their structural complexity and energy dissipating performance. Additionally, it identifies gaps in the current state of the art and highlights the need for further experimental research.

Chapter 2: Dynamic Impact Tester This chapter outlines the design and construction of a new dynamic impact tester inspired by the Charpy impact test. The setup is optimized for simplicity, accuracy, and repeatability, enabling the evaluation of mechanical metamaterials under dynamic impact conditions. The chapter discusses the development methodology, key design decisions, sensor integration, and the measurement technique in detail.

Chapter 3: Energy absorbing metamaterials In this chapter, a series of mechanical metamaterials composed of bistable triangular flexures are fabricated using 3D printing. Both quasi static and dynamic tests are performed to evaluate their energy dissipation capabilities. The effects of key geometric and material parameters, such as flexure angle, geometry, and thickness, are systematically analysed, and relevant performance trends are identified.

Chapter 2

Literature review

2.1 Introduction

The goal of this literature review is to provide a comprehensive overview of non-destructive energy dissipating mechanical metamaterials. By surveying the current state of the art, we aim to identify design principles that govern energy dissipation in these materials. This knowledge can support the development of metamaterials tailored for specific applications, such as structures used in crash absorption systems. And further studies in mechanical metamaterial properties like the coefficient of restitution.

The non-destructive characteristics make these materials reusable. This not only reduces long-term costs but also minimizes environmental impact by decreasing the need for material replacement after collisions.

Preliminary research revealed a gap in the literature: no studies were found that focus explicitly on designing mechanical metamaterials with a specified coefficient of restitution. To achieve this goal, it is necessary to first identify and analyse the design parameters that influence energy dissipation behaviour. While some prior work has investigated specific behaviour parameters such as: material differences Che et al. (2018); snapping sequence of unit cells Giri and Mailen (2021); or topology optimization Chen et al. (2018). Broader relationships between different metamaterial designs and their energy-dissipating performance remain unclear.

This review begins by outlining the common working principles of energy absorbing mechanical metamaterials. We then describe the methodology used to collect and categorize relevant research papers. Following this, we analyse common design strategies found in literature, and rank them according to performance criteria, seeking patterns and insights that can guide future designs.

In conclusion, this review offers a structured summary of key findings and trends in the field of energy-dissipating and energy-storing mechanical metamaterials. We also highlight promising directions for future research, particularly those that could lead to the development of reusable crash-absorbing systems with predefined energy dissipation characteristics.

2.2 Theory background

This section provides a brief overview of the material and mechanical properties that are the focus of this literature review.

2.2.1 Metamaterials

Metamaterials are materials composed of repeating patterns of unit cells, which are typically small, engineered building blocks. These unit cells can modify the behaviour of the overall metamaterial, giving it unique or enhanced material properties. One common property that metamaterials are designed to influence is the Poisson's ratio. Hou and Silberschmidt (2015)

2.2.2 Negative stiffness and bi-stability

Negative stiffness refers to a material that exhibits a negative slope in its stress-strain or force-displacement curve. In metamaterials, negative stiffness is often achieved by exploiting elastic instabilities, such as buckling. When a critical force is applied to a beam, it may buckle and transition from one stable state to another without external intervention. This behaviour is known as bi-stability. A common example of bi-stable materials can be found in the caps of shampoo bottles, which snap from the closed position to the open position after an initial force is applied, allowing the bottle to dispense shampoo without interference. Additionally, metamaterials can be designed with multiple stable states, known as multistable, further enhancing their functionality.

2.2.3 Coefficient of restitution

The coefficient of restitution (denoted as e) is defined as the ratio of the velocity after impact to the velocity before impact. It is closely related to energy dissipation during collisions, with its value constrained to the range $0 \leq e \leq 1$. A coefficient of $e = 0$ indicates a perfectly inelastic impact (no kinetic energy is conserved), while $e = 1$ represents a perfectly elastic impact, where no kinetic energy is lost Haron and Ismail (9 18). A common example of a high coefficient of restitution is a bouncing ball. When dropped from a height of one meter, the ball will nearly return to the same height due to the conservation of kinetic energy, with the ball's velocity being reversed upon impact.

2.2.4 Energy absorption, dissipation, and storage

When a structure is used as an energy-absorbing mechanism, the incoming energy is typically absorbed in one of two ways. The first method is energy dissipation, where the energy from the impact is converted into heat and lost to the surrounding environment. An example of this would be the deformation of a car bumper during a collision, where energy is dissipated as heat through the plastic deformation of the material. The second method involves energy storage, where the energy is temporarily stored as elastic potential energy within the material. An example of this is when a spring is compressed during impact; the energy is stored as potential energy and can later be released when the spring returns to its original shape.

2.3 Constraints and categorization

This section outlines the process of identifying relevant papers and the methods used to analyse and compare them.

2.3.1 Search string method

Before providing a comprehensive overview of the state of the art in energy-dissipating and energy-storing mechanical metamaterials, an initial search was conducted to identify relevant search terms. The initial search was focused on the coefficient of restitution, but due to a lack of papers specifically discussing the coefficient of restitution in combination with (mechanical) metamaterials, the literature review was broadened to encompass a wider scope of energy dissipating and storing (mechanical) metamaterials. The energy dissipation and storage search resulted in a set of search terms, which were then categorized into separate groups. Using Boolean operators, these terms were combined to create a wide range of search strings. These strings were subsequently used in the Scopus database to retrieve relevant papers. The search strings used can be seen in Table 2.1. The first column contains synonyms for metamaterials, ensuring that all papers related to metamaterials are included in the search scope. The second column lists the desired optimized or analysed material properties, narrowing the search to papers that focus on energy dissipation and related properties. The third column includes mechanical principles by which the material properties can be altered, further limiting the scope to mechanical metamaterials. Finally, the last column is designed to exclude papers from unrelated fields of study, ensuring that only research related to mechanical metamaterials is included.

	AND			AND NOT
OR	Metamaterial	Coefficient of restitution	Bistable	Asphalt
	Tiled	Energy absorption	Bistability	Acoustics
	Architected	Impact	Multistable	Vibrations
	Truss structure	Viscoelastic	Multi-stability	Nano
	Tensegrity structure		Snap	Concrete
			Inertial	
			Bucking	
			Morphing	

Table 2.1: Combination table of search terms used in the Scopus search string

The search string, applied in Scopus on 3-09-2024, yielded a total of 167 papers. Of these, two were in an incomprehensible language, 12 were unavailable, and 36 were deemed irrelevant to the desired mechanical metamaterial study. The remaining 117 papers were analysed to assess the state of the art in mechanical metamaterials. The analysis focused on the following properties: the complexity of the materials, the bi-stability or multi-stability of the material, and the energy dissipation and storage characteristics exhibited by the material.

2.3.2 Complexity rating

To create an overview and comparison of the different metamaterials in the literature, a custom metric was developed. The complexity of each material was rated using a counting method, where each beam or component of the metamaterial was assigned a numerical score. The sum of these scores provided the overall complexity rating of the metamaterial. This rating was

based on the smallest possible unit cell that could be constructed for a metamaterial. Regular beams were assigned a score of 1, while beams designed to be bi-stable were rated 2. More complex components received higher scores accordingly. Additionally, a multiplier was applied if the design was used in multiple axes or revolved around a single axis. An overview of these complexity scores can be seen in Table 2.2.

	Complexity score	Multiplier
Regular beam	1	
Bi-stable beam element	2	
Spring element	3	
Latching connection	3	
Magnets	3	
Revolted around one axis		X2
Reused in two axes		X2
Reused in three axes		X3

Table 2.2: Score system to rate the complexity of metamaterials

2.3.3 Bi-stable snap trough flexures

Bistability can be a useful mechanism for storing energy from impacts. To differentiate papers that use bi- or multi-stability, the studies are categorized according to their stability type. While bi- or multi-stability can occur in any beam within a system, this labelling only considers beams that are intentionally designed to be bi- or multistable. Bistability is analysed as follows: if the material exhibits bi-stability using either a negative stiffness beam or snap mechanism in one cardinal direction, it is labelled as bi-stable. If the material is bi- or tri-stable in multiple cardinal directions, it is labelled as bi- or tri-way bi-stable. Materials that exhibit multi-stability are marked as multistable.

2.3.4 Energy Absorption, dissipation, and storage

Finally, a comparison was made of the energy absorption capabilities of the metamaterials. Within the scoped papers, the following classifications were made: papers that did not mention energy absorption capabilities; papers that only measured the energy dissipated during compression; and, lastly, papers that analysed both compression and extension of the metamaterials, providing insights into the energy dissipation and storage capabilities. To gain a better understanding of energy dissipation, it is essential that both compression and extension are measured. Without these measurements, it is impossible to differentiate between energy lost due to dissipation and the energy stored as elastic potential energy. In cases where both measurements were available, the estimated energy dissipation was also noted.

2.4 Results

This section presents the key findings and notable results from the analysis of the selected papers.

2.4.1 Complexity and bi-stability of the metamaterials

First, the complexity of the structures was analysed, with the results shown in the histogram in Figure 2.1. The complexity of each structure was rated according to the system outlined in Section 3. Based on these complexity ratings, different designs were grouped accordingly. The following section provides an overview of the various mechanisms used for energy dissipation and storage.

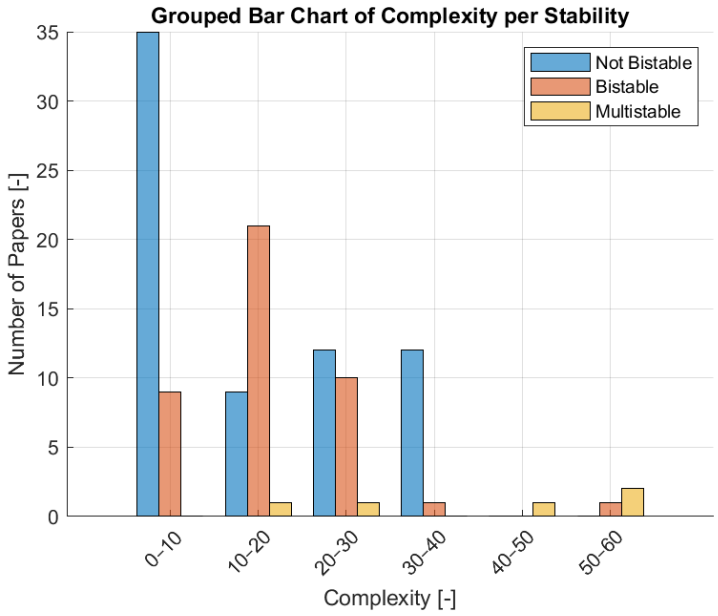

Figure 2.1: Number of papers per complexity, grouped into ranges of 10, separated by stability type.

Low Complexity (< 10) **and not bistable** This category focuses on fine, repeating microstructures that do not incorporate bistable components. The metamaterial structure is typically composed of planes or struts arranged in a repeating grid pattern, often based on geometric shapes such as triangles or hexagonal prisms. These metamaterials generally exhibit multiple degrees of freedom. They are primarily used to achieve a lower strength-to-density ratio compared to the parent material and to enhance energy dissipation capabilities through internal buckling. Examples of such structures can be seen in figure Figure 2.2.

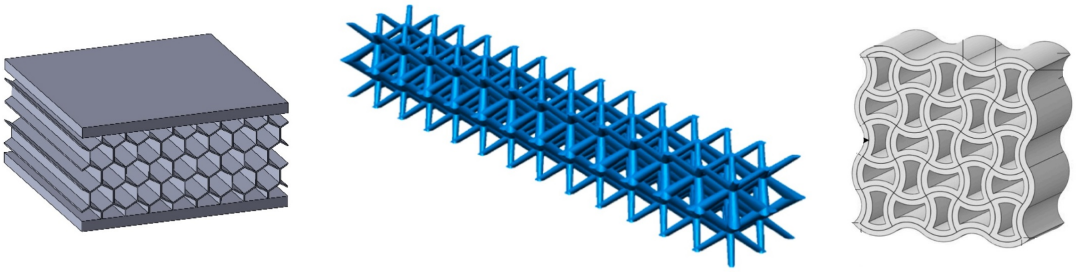

Figure 2.2: Simple geometric patterns observed in both structures, from left to right: Yazdani Sarvestani et al. (2018), Nian et al. (2023), Biffi et al. (2024).

Low Complexity (< 20) **and bistable** This category includes the first bistable structures, which typically follow a triangular design featuring two bistable flexure beams. The main variations between these structures lie in the angles of the flexures and the stacking pattern of these mechanisms. A selection of different variations can be seen in Figure 2.3. The working principle of these flexure triangles revolves around the two bistable flexure beams. During loading of the metamaterial, the beams will snap through to their second bistable orientation. This occurs due to the negative stiffness of the beams, creating a second stable point in the mechanism. The negative stiffness can be viewed as a method of energy storage.

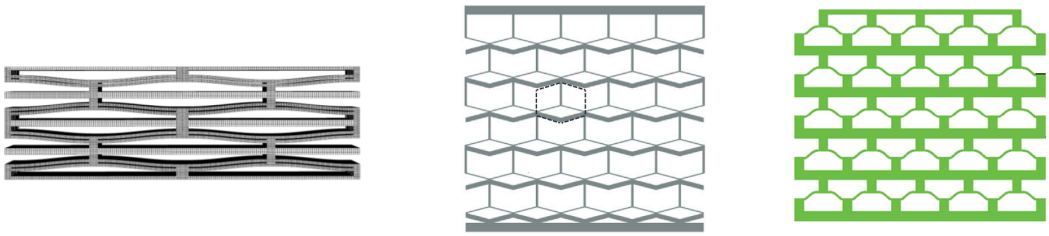

Figure 2.3: Various configurations of bistable triangles, from left to right: Jafarabadi et al. (2023), Meng et al. (2020), Che et al. (2017).

Complexity (10-20) not bistable At a higher complexity level, non-bistable structures evolve into truss structures, which are primarily applied in sandwich panels. An overview of these structures can be seen in Figure 2.4. The working principle of these metamaterials is to reduce density while maintaining as much stiffness as possible in the panel, resulting in lighter structures compared to the parent material. These structures are particularly useful in panels that can withstand more compression than conventional sandwich panels.

A second variation is the rotating squares structure. These structures resemble the low complexity non-bistable structures but are rated with higher complexity due to the added constraints, making the mechanism a single degree of freedom in a two-dimensional spanning metamaterial. An example of this design can be seen in Broeren et al. (0 02).

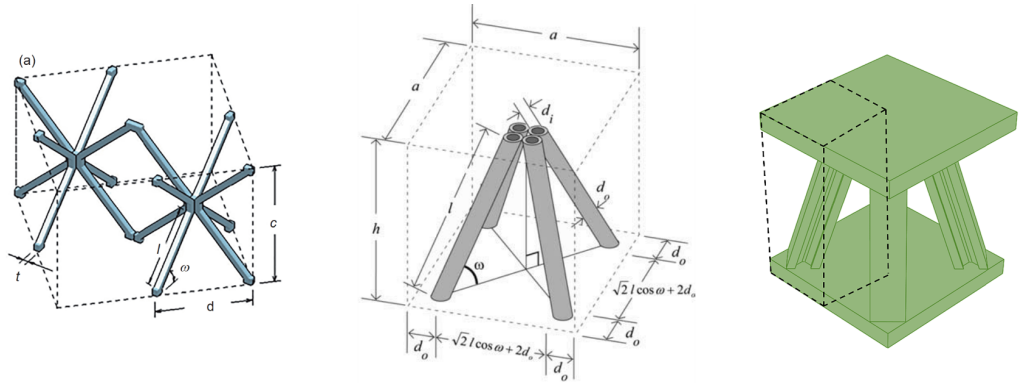

Figure 2.4: Overview of medium-complexity non-bistable structures, from left to right: Feng et al. (2020), Queheillalt and Wadley (2011), Uddin et al. (2024).

Complexity 36 - tensegrity structures An outlier in the complexity rating is a structure with a rating of 36, which corresponds to spherical tensegrity structures. These structures are surprisingly often used for this application, an example is shown in Figure 2.5. The primary advantage highlighted by most studies is their high strength-to-weight ratio, making them particularly suitable for aerospace engineering applications. Other papers that feature similar structures include Pajunen et al. (2019), Garanger et al. (2021), and Zhang et al. (2021).

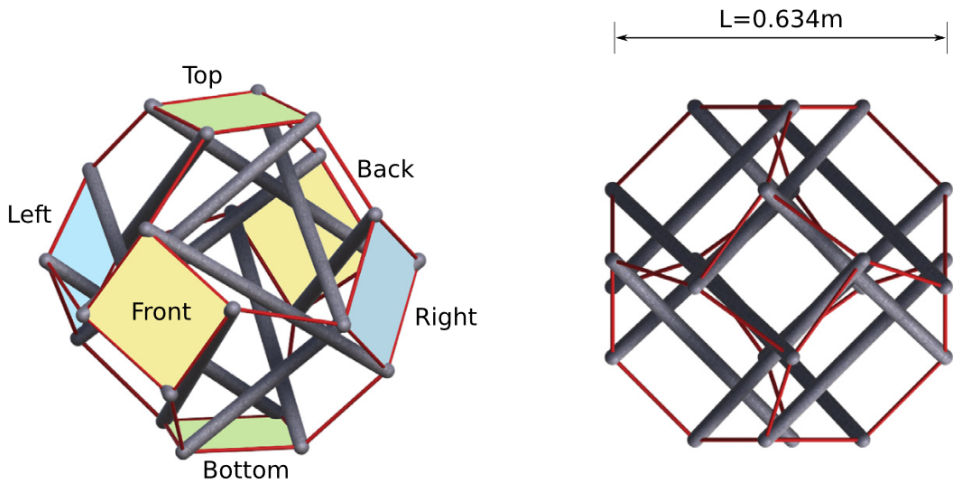

Figure 2.5: A commonly used tensegrity structure: Rimoli (2018).

High complexity (> 20) **not bistable** This section focuses on structures that build upon the simplicity of lower complexity non-bistable designs, but over-constrain them to the point where the deflection of the system is coupled with uncontrolled flexing of all construction members. The high complexity-rated non-bistable structures are generally large lattice structures. Some examples can be seen in Figure 2.6. These structures are capable of achieving specific mechanical properties while maintaining relatively low weight. Additionally, a 3D variation of the rotating cubes can be found within this complexity range. However, it has a high complexity rating due to the need to constrain the system to a three-degree-of-freedom design. An example of this can be seen in Shen et al. (2015).

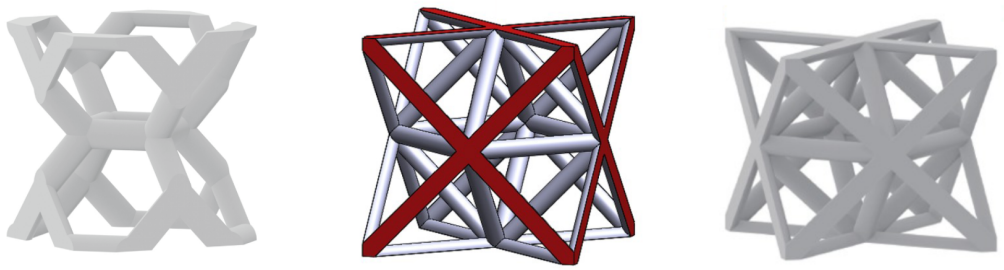

Figure 2.6: Examples of over-constrained structures, from left to right: Tian et al. (2024), Osman et al. (2020), Li et al. (2023).

High complexity (> 20) **and bistable** For the bistable variation, the similarity to the 2D version is also evident in the 3D structures. Some examples can be seen in figure Figure 2.7. The primary functionality of these structures remains the same as the simpler 2D version, but they are created in 3D. This can be achieved either by revolving the structure to form dome-shaped configurations or by combining multiple 2D structures to achieve stability in 3D.

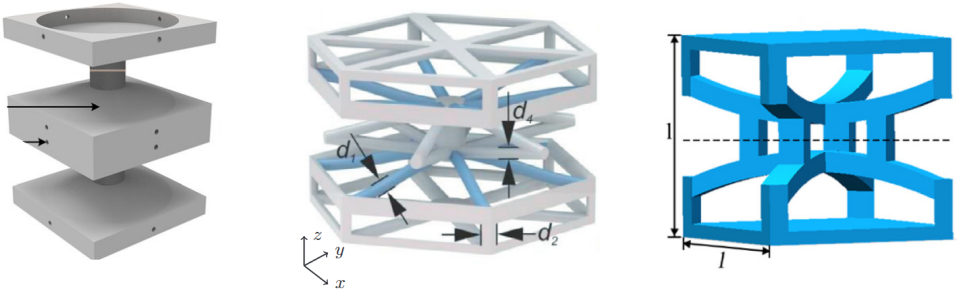

Figure 2.7: Different variations of the triangle flexure, maintaining the same functionality but in 3D, from left to right: Tan et al. (2023), Findeisen et al. (2017), Yang et al. (2024).

2.4.2 Special interesting cases

In addition to storing energy in the elasticity of beams or planes within the material, several other principles are explored in the existing literature. This section will highlight some innovative solutions.

Magnetic springs One alternative method for storing energy is the use of magnets, which was explored in two studies. The first study combined magnets with bistable flexure triangles to enhance the negative stiffness effect of the metamaterial Chen et al. (2019). The second study utilized magnets as a negative stiffness mechanism by strategically positioning them Tan et al. (2019). An illustration of both design can be seen in figure Figure 2.8.

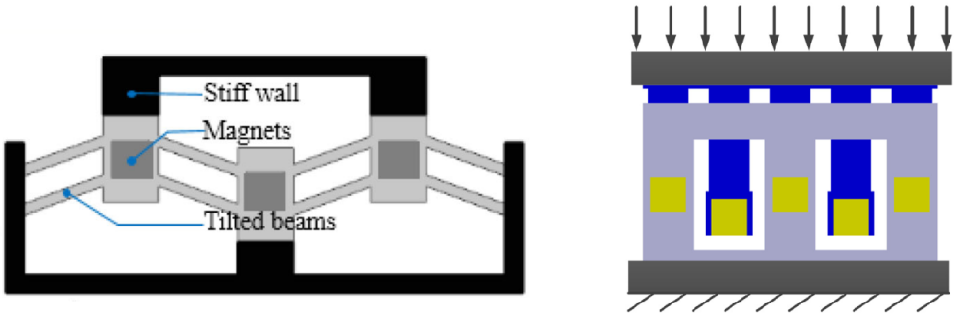

Figure 2.8: On the left, a flexure triangle with added magnets Chen et al. (2019), and on the right, a standalone magnetic energy absorber Tan et al. (2019).

Spring-loaded and latching structures The following set of papers examines a mechanism that combines spring-like structures in the material materials with latches to achieve both impact-absorbing capabilities and multistable behaviour. While these innovative solutions provide new approaches to designing metamaterials, the line between these mechanisms and true metamaterials becomes increasingly blurred. A selection of these mechanisms is shown in Figure 2.9.

Other metamaterial designs used are snap-fitting mechanisms, which mostly consist of pins that latch when the structure gets compressed Chen et al. (2023), Xu et al. (2023). Although these systems perform well, their recoverability is lacking, depending on the design.

The following set of papers explores a mechanism that combines spring-like structures within metamaterials with latches to achieve both impact-absorbing capabilities and multistable behaviour. The spring-like structure facilitates high energy storage, while the snap-fitting mechanisms, which primarily consist of pins that latch when the structure is compressed, contribute to the system's ability to absorb impacts. While these innovative solutions offer new ways to design metamaterials, the distinction between these highly complex mechanisms and single material metamaterials becomes increasingly blurred. A selection of these mechanisms is shown in Figure 2.9.

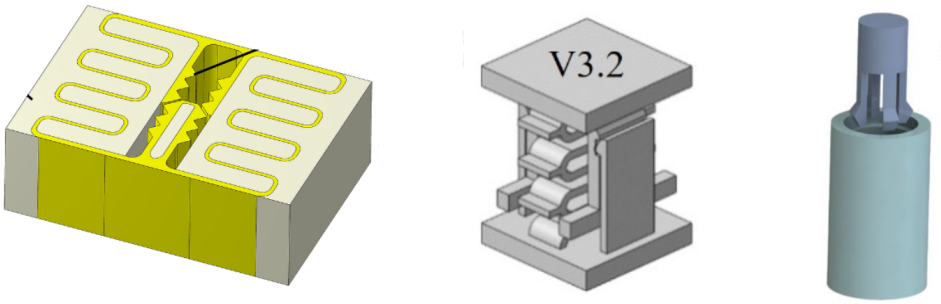

Figure 2.9: Different spring and snapping mechanisms, from left to right: Chen et al. (2023), Kappe et al. (2022), Xu et al. (2023).

Origami structures A completely different approach involves using origami to create the structure. The main advantage of these metamaterials is the simplified construction, which arises from the constraint of creating a mechanism from a flat sheet of material. Two origami patterns are shown in Figure 2.10.

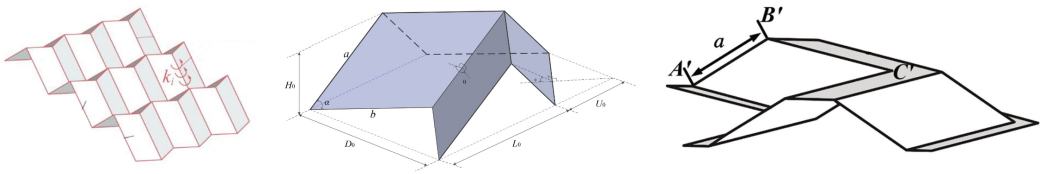

Figure 2.10: Two different origami patterns used for impact absorption, from left to right: Li et al. (2019), Karagiozova et al. (2019), Qiang et al. (2024).

Inserts in the mechanical structures The next interesting approach to achieving new characteristics involves inserting additional materials into the structure of commonly used metamaterial designs. Most of these metamaterials incorporate foam to enhance energy dissipation Yao et al. (2024b). Various methods of foam incorporation can be observed, such as using triangle flexure mechanisms filled with foam Yao et al. (2024c), Tan et al. (2022), or other foam-oriented solutions like the architected lattice structure studied in Wang et al. (2019). Additionally, different materials, such as those used in Montanari et al. (2023), introduce elastic inserts that further increase energy dissipation. These inserts can significantly alter the overall material characteristics of the metamaterials.

Lattice structures Another commonly used material is a form of lattice structure. The beams in these lattice structures are designed to flex under load, allowing them to absorb energy. These structures are primarily used for energy absorption applications and typically exhibit higher dissipation levels, ranging from 50-75 % Zhang et al. (2018), Mohan et al. (2017).

2.4.3 Energy absorption, dissipation and storage

This section will highlight the energy absorption characteristics of the state-of-the-art in energy-absorbing metamaterials.

Within the search results, a distinction was made between papers that measured energy dissipation during the loading of the metamaterial, papers that also measured the unloading energy, and papers that measured neither. Of all the papers, only 29 measured both the loading and unloading phases of the metamaterial. Measuring both phases is crucial, as it allows for the differentiation between dissipated and stored energy. This can be done by calculating the energy difference between the compression and decompression cycles. Achieving zero dissipation would be ideal for applications where energy recovery is essential, as it minimizes energy losses. On the other hand, 100 % dissipation would be beneficial for applications requiring effective energy absorption, ensuring that all the energy from the impact is absorbed, preventing rebound, and reducing the risk of further damage.

Within these 29 papers, the dissipation versus energy stored percentages were analysed and can be observed in Figure 2.11. The percentages of dissipation are based on one of the following three methods. First, if the paper provided direct measurements of both the loading and unloading energy, the dissipated energy percentage could be easily calculated. The other two methods involve estimating the energy difference by examining the area under either the force-displacement curve or the stress-strain curve. These areas were manually analysed by comparing the corresponding regions under the curve.

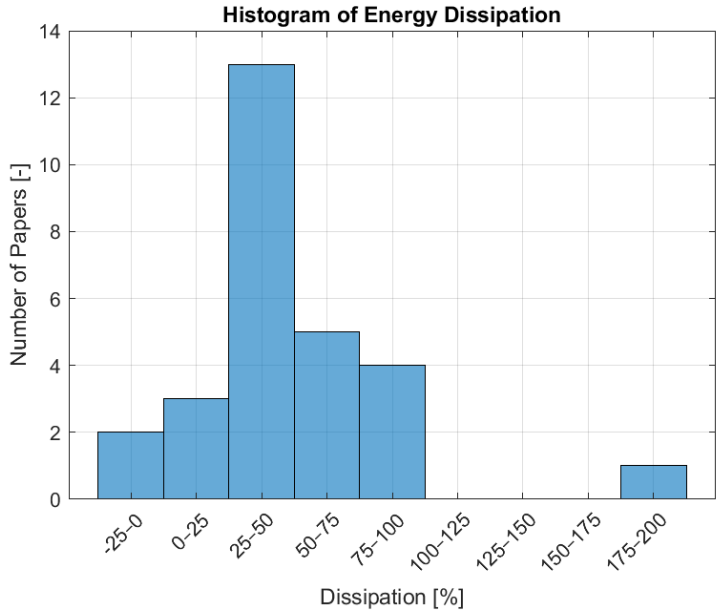

Figure 2.11: Percentage of energy dissipation versus the number of papers in each percentage range, grouped in intervals of 25.

Outliers An unusual observation is the presence of negative energy dissipation in one of the metamaterials, which should not be possible under normal circumstances. However, in the case of Liang et al. (2024), an external energy source is applied to the material to heat it, causing the decompression energy to be higher than the compression energy.

Another interesting case is the energy dissipation exceeding 100 %. This is seen in Haghpanah et al. (2016), where the energy required to compress the metamaterial is fully dissipated, and then during the returning movement, the same amount of energy is required again. This results in a total dissipation exceeding 200 %, effectively dissipating all of the input energy in two directions.

2.4.4 Energy dissipation performance

With the remaining results, one mechanism reappears frequently: the bistable triangle flexures. These come in different shapes and sizes and exhibit dissipation values ranging from as low as 10 % to as high as 100 %. The difference in dissipation appears to be due to the various designs of the flexures. A low-dissipating triangle flexure is typically oriented more vertically Hou et al. (2023), compared to the more horizontally oriented flexures Jafarabadi et al. (2023). In Figure 2.12, the relation between the angle of the flexure and the dissipation can be observed. While a correlation between the angle of the triangle flexures and dissipation seems to exist, there is insufficient data in the current state of the art to draw definitive conclusions on this relationship.

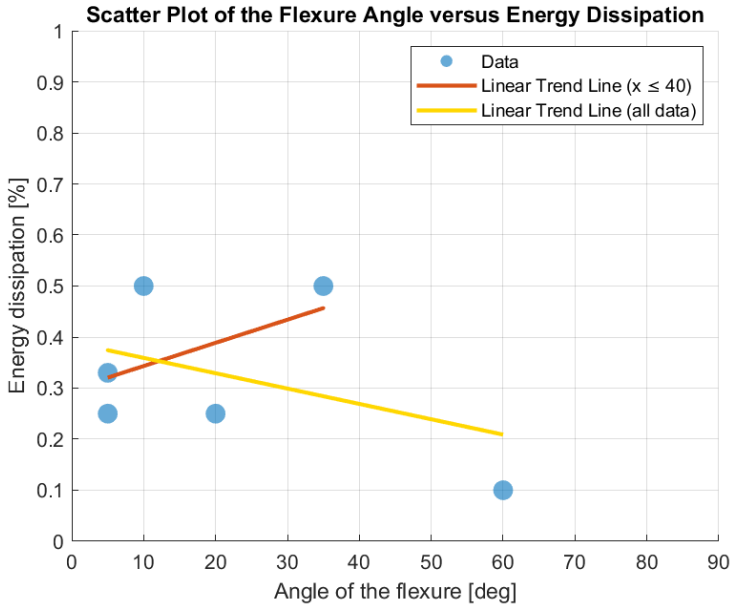

Figure 2.12: The plot of the flexure angle versus energy dissipation suggests a positive relationship between the angle and energy dissipation for angles up to 40 degrees, while an inverse relationship is observed for all available data points. However, due to limited data points, the overall trend may not be fully representative.

Another trend indicating higher dissipation appears to be related to the repeating nature of the metamaterial. Specifically, having more layers results in higher overall dissipation. The paper Giri and Mailen (2021) demonstrates this relationship for the triangle flexures used, while other studies that test multi-layered metamaterials also show an increase in energy dissipation related to having more layers.

2.5 Discussion

This section discusses the overarching results and potential gaps revealed by this literature review. Additionally, critical observations regarding the research methodology will be addressed.

2.5.1 Literature results

The initial research goal was to identify metamaterials with designed coefficients of restitution. However, the literature review revealed that little to no research has been conducted in this specific direction. To broaden the scope, the material characteristics related to the coefficient of restitution namely, energy absorption and dissipation were considered. Thus, this literature review focused on the energy dissipation and storage capabilities of mechanical metamaterials, providing an overview of these materials. It also aimed to determine which design parameters are important for the creation of energy-absorbing and storing metamaterials, and, consequently, for the design of metamaterials with a desired coefficient of restitution.

Of particular interest were the bistable triangle flexures. Numerous papers presented different designs, varying in parameters such as size, material, angle, and measurement methods. These variations led to significant differences in the measured energy dissipation and storage. However, with fewer than ten papers having measured both energy storage and dissipation, comparisons between the results remain limited. Gaining a comprehensive understanding of the parameters of energy dissipation and storage capabilities of bistable triangle flexures could be a crucial step toward systematically designing metamaterials.

Within the parameters of energy dissipation and storage, an interesting question arises: What are the minimum and maximum achievable energy dissipation and storage for a bistable triangle flexure? By considering a specific set of parameters and a selected group of parent materials, this question could offer valuable insights. This research gap presents an opportunity to explore how the design of these structures influences their energy absorption and storage capabilities. Addressing this could be a next step in the study of energy absorbing metamaterials.

2.5.2 Selection method

The use of search strings in this process was to get an overview of all mechanical working principles of energy-absorbing metamaterials. The results, in general, seem to provide a broad overview of possible designs for energy-absorbing mechanical metamaterials, with no mechanisms being over-represented in the results. However, there does seem to be a slight preference for simpler designs, as can be seen in Figure 2.1. While this is useful for understanding the state of the art, more specific search strings that focus purely on the flexure triangle structures might yield more information about these particular designs. This could be in the form of studies on bistable beam flexures, for example.

2.5.3 Categorisation criteria

While the categorization works to provide an overview of the different types of designs and how their working principles relate to one another, their performance categorization could be made clearer due to the lack of a clear performance index. A good performance index is difficult to apply because most papers focus on different applications and testing methods. Furthermore, only a few papers actually measured both the energy absorption and storage of the metamaterials. These papers allowed for a more detailed categorization and yielded a more performance oriented

comparison. However, due to the limited number of papers, no statistically significant trends can be identified between their properties and performance indexes.

2.5.4 Energy dissipation metamaterial versus parent material

The intuitive correlation between the energy dissipation of a metamaterial and the energy dissipation of its parent material can significantly influence the measured energy dissipation. While there is likely a strong relation, the design of a metamaterial also influences this dissipation, as demonstrated in Gavazzoni et al. (2022). This indicates that the design of a metamaterial can indeed alter its energy dissipation capabilities.

2.6 Conclusion

This literature review aims to inform about the different metamaterials used in the design of energy absorbing and storing metamaterials. The overview provided highlights the complexity and design directions found in the papers, resulting in a wide range of designs. However, there appears to be a limited focus on energy storage and energy diffusion. Most of the studied papers primarily focus on the total dissipated energy of the metamaterials, without considering the stored energy. The few papers that do measure both dissipation and storage typically measure the full energy cycle. Among these papers, there is a significant variation in the energy dissipation and storage capabilities of metamaterials. This leaves a gap in understanding the relationship between the design properties of a metamaterial and its energy dissipation and storage capabilities. Future research could focus on expanding knowledge about the connection between the design of energy-dissipating and energy storing metamaterials. This would help identify which parameters are most useful for the design and application of metamaterials.

Chapter 3

Dynamic Impact Tester

3.1 Introduction

This chapter details the methodology used for testing and developing energy absorbing metamaterials, focussing on the development of a new dynamic impact tester. Generally, two different testing methods can be used for evaluating the energy absorbing characteristics of these materials: Quasi static compression testing and dynamic impact testing. This chapter will first describe the quasi static compression testing method and then provide an overview and analysis of various dynamic impact tests. Ultimately, introducing a new energy absorption tester based on the simplicity of the Charpy impact test. In chapter 4, both testing methods will be used to characterize the energy absorbing capabilities of mechanical metamaterials.

Traditional methods for testing energy absorption, including quasi-static compression and various dynamic impact tests, often present limitations. While quasi static methods allow for precise force measurement, they fail to capture the material's behaviour under high-velocity impacts, which are more representative of real-world energy absorbing scenarios. On the other hand, the widespread adaptation of dynamic impact tests is currently limited. This is primarily due to the complexity of its construction, lack of standardized testing setup, and challenging data acquisition that often rely on complex measuring methods. Consequently, using a dynamic testing setup can be time-consuming and expensive, leading to their less frequent use in research.

This work aims to introduce a new testing method that balances accessibility, complexity, and precision, bridging the gap between low-velocity quasi static testing and complex dynamic impact testing methods

The following sections outline the approach behind our design. It begins with a description of commonly used quasi-static and dynamic testing methods. The dynamic tester design section then describes the conceptualization, system requirements, and construction process, while the measurement system section details the data acquisition and analysis methods used. Finally, the discussion evaluates the capabilities and accuracy of the developed system and highlights areas for future improvement.

3.2 Energy absorption testing methods

This section will give an overview of commonly used methods of measuring energy absorbing materials, and relevant other measurement methods. Which are either used as a basis of design, or are used in the testing in chapter 4.

3.2.1 Quasi static testing of energy absorbing materials

Quasi-static testing, also named displacement controlled compression, is a method of testing which is done on a tensile testing bench. With the drawback of being a low velocity approach of the dynamics of the material. An advantage of this testing method is that the forces can be measured accurately. This method is commonly used in the testing of energy absorbing mechanical metamaterials, some papers that use quasistatic testing are Ju et al. (2024), Jafarabadi et al. (2023) and Zhang et al. (2024). This is due to the slow speed, making critical failures easy to observe, and the wide availability of this test setup in academic environments. The tensile testing setup used is a Zwick Roell Z005, with a maximum test load of 5 kN, and maximum crosshead speed of 3000 mm/min. A sample clamped in the tensile tester can be seen in Figure 3.1.

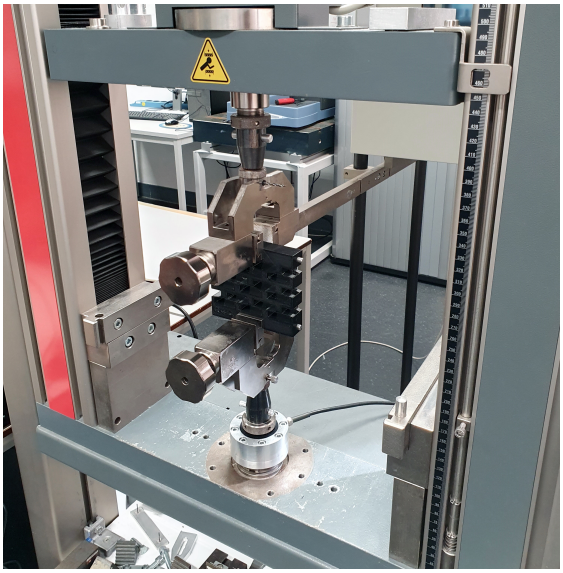

Figure 3.1: A black TPU sample in the Tensile testing setup, used for the quasi static measurements.

The testing methods worked as follows; First, the sample material is clamped between the tensile tester. After which the tensile tester will move a predefined displacement. The length of this displacement is a function of the compression capability of the material, the speed is set at 300 mm/min. This displacement cycle contains a compression and extension phase. During this displacement, the force required for the displacement is measured. The total force displacement over the compression and extension cycle can be calculated to get the energy absorbed, and the energy returned, respectively. This difference is used to calculate the energy dissipated by the material. An example of the data obtained in a quasi static test can be seen in Figure 3.2.

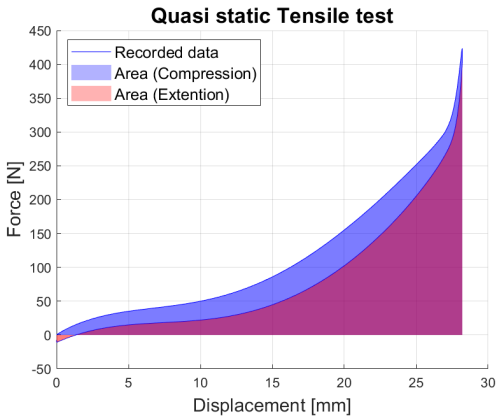

Figure 3.2: Example of the quasi static test data, with the area under the curve marked in blue for the compression phase, and marked in red for the extension phase.

3.2.2 Dynamic testing of energy absorbing materials

The quasi static testing method has the limitation of only being in the low velocity range. To study high velocity impacts, dynamic testing is done. Which is closer to the real-life applications of energy absorption. One well known example is the testing of the impact structure of vehicles, which is done by crash safety tests Smith (1981). Within the studied papers in chapter 2, multiple different methods of dynamic energy impact can be found. This section will give an overview of the different dynamic impact testing methods.

The most simple method of testing dynamic energy absorption, is by dropping the material itself from a set height and measuring the bounce back. This is mostly done by taking videos of the setup. An example of the use of this method can be found in Yao et al. (2024a). The advantage of this method is that there is limited needed testing equipment. The main part needed is a camera to register the test, after which the bounce height can be measured using video analysing software. The disadvantages of this method are that the trajectory of the material is not defined. Any imperfections in the material contact surface or drop position will cause undesired rotations within the sample. Another disadvantage is that the impact energy absorbed by the material is always the same as the material weight multiplied by the gravitational acceleration.

The second method used for energy absorbing testing is dropping the material using a guide rail, or dropping a weight on the material also using a guide rail Xiao et al. (1 02). With the use of these rails, the orientation and impact velocities can be fixed, which increases accuracy and repeatability. Also, other measurement methods than a camera can be used by for example adding a contact force sensor, or an acceleration sensor, simplifying data collection. While this is a general improvement, the complexity of using linear bearings in impact absorbers can lead to misalignment or failure, in addition to increasing the overall cost of the system.

3.2.3 Charpy impact test

The Charpy impact test was invented in 1900 by Georges Augustin Albert Charpy, and is a commonly used test to quickly measure the relative toughness of a material. It measures the energy absorbed by a standardized, notched specimen which fractures under a fixed impact load. In the test, a hammer mounted on a pendulum strikes the specimen, which is fixed in place

between two supports. As the hammer strikes the sample, part of the kinetic energy is absorbed by the material. The remaining energy is indicated by the height of the pendulum after impact, which is used to calculate the absorbed energy. Saba et al. (2019).

While this test is effective in quantifying the energy absorption, its primary purpose is to measure a material's toughness. Besides this, it inherently a destructive test, making it unsuitable for applications where repeated testing of the same sample is desired. Which is the case for the materials in chapter 4, where non-destructive testing is preferred to be able to measure repeatable performance.

Aside from the destructive nature of this test, it offers several advantages in terms of construction. It is mechanically simple, consisting of a single pendulum and a support frame, which makes the Energy measurement reliable and consistent. This simplicity makes it a strong foundation for developing a new impact absorption tester, the details of which will be discussed in the following section.

3.3 New dynamic tester design

This section outlines the design steps taken to develop a simplified testing setup for evaluating dynamic impacts, based on the Charpy impact test.

3.3.1 Inspiration for the design

Most existing designs for dynamic energy absorption tests are either difficult to manufacture, due to the use of sliding bearings and or measuring of the impact forces, and or have hard to analyse measurements, relying on complex video-based measurement techniques. To address these issues, a new method is introduced based on the Charpy impact test.

The simplicity of the Charpy impact test, consisting of a single pendulum mounted hammer, served as the base for the new design. This configuration results in a simple mechanical structure, that still provides a fixed and controlled motion path. As a result, the design minimizes both cost and mechanical complexity, making the setup easy to construct, operate, and reproduce. A visual of the newly designed tester can be seen in Figure 3.3.

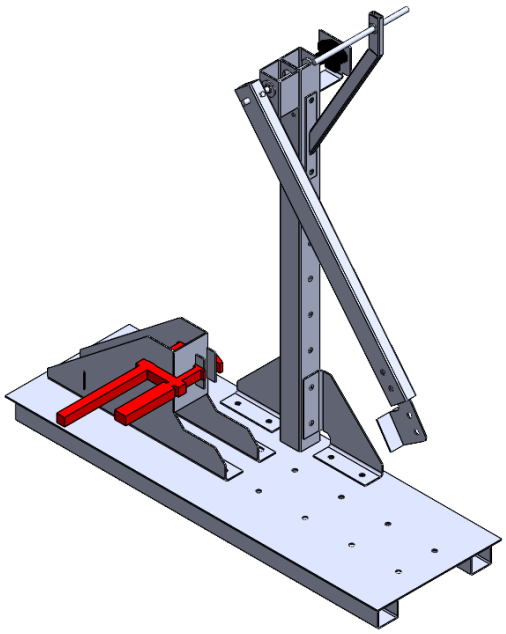

Figure 3.3: The full design of the dynamic tester, for the testing of energy absorpting materials.

3.3.2 Selection of the design

A comparison of various dynamics test methods from existing literature and the new Charpy inspired testing setup, is presented in Table 3.1. Each test is evaluated based on five criteria: construction complexity, relating to the difficulty of aligning components and moving parts; measurement complexity, concerning the complexity of data acquisition; test repeatability, referring to how easily the test can be repeated; measurement precision, focused on the level of noise and variability in the recorded data; and finally overall cost, covering both construction and measurement system expenses.

Test type:	*Construction complexity*	*Measurment Complexity*	*Test Repeatability*	*Measurment Precision*	*Cost of setup*	*Total*	Ref
Sample drop test	++	–	–	-	++	-+	Yao et al. (2024a)
Guided rail Sample Drop test	-	+	+	+	-	-+	Xiao et al. (1 02)
Guided rail Weight Drop test	-	+	+	+	-	-+	Chen et al. (2023)
Charpy inspired Drop test	+	+	++	+	+	+	Presented solution

Table 3.1: Overview of the different Dynamic impact test methods.

Among the evaluated methods, the Charpy inspired impact test consistently performs well in terms of simplicity of construction, ease of measurement, repeatability, and cost-efficiency. However, it is limited by the measurement precision, which has the potential of resulting in inaccurate data within the measurements. Given its overall advantages in the other categories, the Charpy test was selected as the basis for the simplified dynamic impact testing setup, with the objective of improving upon traditional weight drop tests in terms of easy of use and measurements complexity.

3.3.3 System Requirements and Impact Force Calculation

The system prioritizes ease of construction and ease of measurement. The baseline design uses a 1 kg mass on a hammer arm with a length of 0.5 m, making it have a potential height of 1 m. This setup yields a total peak force of a 1000 N.

To calculate the maximum impact force, we assume that the total potential energy PE of the falling mass is fully converted to kinetic energy at the moment of impact. This energy is then absorbed over a minimum distance of 0.01 m, resulting in a peak force of a 1000 N. Without assuming this minimum displacement, the theoretical maximum impact force would approach infinity. An example of this would be using a solid block of steel as a sample, which would exhibit a near-zero displacement, which would likely lead to deformation of the test setup, therefore using non-deforming samples on this dynamic impact tester needs to be avoided.

First, calculate the potential energy (PE):

$$PE = mgh = 1\,\text{kg} \times 10\,\text{m/s}^2 \times 1\,\text{m} = 10\,\text{J} \tag{3.1}$$

Then, determine the impact force (F):

$$F = \frac{PE}{\Delta d} = \frac{10\ \text{J}}{0.01\ \text{m}} = 1000\ \text{N} \tag{3.2}$$

These calculations confirm the peak impact force of a 1000 N. This force is subsequently used for the dimensioning of the Charpy inspired Impact test.

3.3.4 Concept of Dynamic impact test

The design of the Dynamic impact test draws inspiration from the Charpy impact test, specifically the simple pendulum mechanism with a hammer. This approach creates a straightforward design with a single degree of freedom. Which simplifies the motion constraint and measuring method. However, the key difference lies in the returning stroke of the Dynamic impact test. Unlike the Charpy test, which typically destroys the sample by striking through it, in this test the hammer changes direction entirely before and after impact. To achieve this capability, a significant reduction of the total mass of the pendulum was needed. Furthermore, the sample holder had to be modified to securely hold the sample in place under the full impact energy applied. Finally, the measurement system also needed to be redesigned, while the original measurement system could only measure the top of the stroke of the path after striking through the sample, our test focusses on capturing the top of the return stroke of the hammer after impact. With these fundamental changes, and the before mentioned force requirements in mind, the final design was developed.

3.3.5 Construction of Dynamic impact test

The design consist of four main parts:

- Frame: Provides the structural support and includes the pole for the mounting of the hammer.
- Hammer: Swings on one axis to generate the impact on the test samples.
- Sample holder: Clamps and supports the test sample.
- Measurement system: Records data during the impact test.

An overview of the parts can be seen in Figure 3.4.

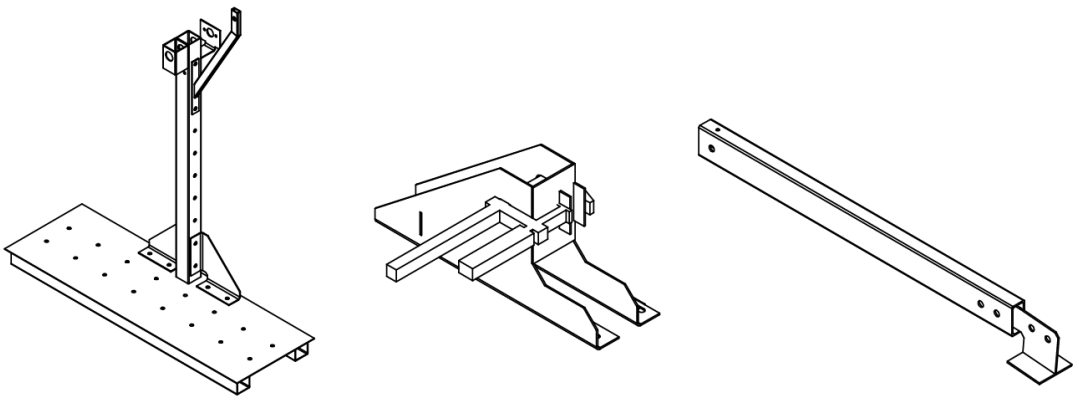

(a) (b) (c)

Figure 3.4: a) The frame of the dynamic tester is designed for high stiffness, with a removable vertical section for convenient storage. b) The sample holder uses a vice clamp and is secured to the base with multiple slotted bolts. c) The impact arm allows for additional weights to be mounted on the hammer head to adjust the impact energy.

For the test setup, steel was chosen as the primary material. This decision was based on its easy availability and its predictable fatigue behaviour under the high impact loads generated by the pendulum hammer. Additionally, steel's relatively low cost makes it an economical choice for construction. While some deformation might occur in certain parts due to the intense impacts, the dimensions of all critically loaded steel sections are specifically designed to withstand a peak impulse force of 1000 N.

The frame is constructed from a simple beam structure, reinforced with stiffeners in the direction of the highest impact force. The vertical beam that support the pendulum is specifically designed to withstand the impact force, by verifying a maximum deformation of 0.5 mm under a 1000 N impact load. At the top of the vertical frame pole, an assembly securely holds the pendulum shaft with bearings that in turn mounts the pendulum hammer. This top assembly also provides a mounting bracket for the measuring system and a flexible mounting system to support the hammer in its initial position before release.

The hammer has a radius length of 0.5 m, measured from the centre of its contact surface to the axle where the pendulum arm mounts to the top of the frame. A key feature is its interchangeable head, of which its current design includes additional mounting points. This gives the possibility to increase the pendulum hammer's weight for samples with higher stiffness, or replace the entire head if a different impact surface is needed for a different test in future research.

The current designed impact surface is a 50x50 mm^2 plate. This dimension was selected to ensure the impact force is applied to the central region of the mechanical metamaterial being studied, thereby minimizing edge effects during impact. The hammer structure, including its head, weighs approximately 1 kg. This relatively heavy arm is the result of the maximum allowed displacement under the impact force of a 1000 N.

The sample holder is responsible to securely hold the sample securely while effectively transferring the impact forces. To hold the sample a vise-clamp is used, which only function is to keep the material in-place, it does not need to transfer the forces to the sample holder itself. Instead, these impact forces are directed through a backplate positioned behind the sample, which in turn transfers the force to the base of the testing setup.

The mechanical metamaterials being studied, as detailed in chapter 4, have approximate dimensions of 100x100x20 mm^3. The varying design parameters of their internal flexures mean that individual samples can have different lengths. To ensure consistent measurements, the entire sample holder can be adjusted along the bottom of the frame, allowing the initial impact position to always be at the lowest point of the pendulum's stroke.

3.4 Measurement system of dynamic tester

The original Charpy impact test setup relied on an analogue measurement system consisting of a needle, that gets pushed by the impact hammer, which would then remain at the peak of the hammer's swing. This method is effective for destructive tests where the hammer continues its path through the sample. However, for this Dynamic Impact Test, this analogue approach is unsuitable because the hammer's direction changes after impact, meaning the needle would not accurately track the return stroke.

To overcome this limitation, a Cherry magnetic rotation sensor is implemented. A spec sheet of this sensor can be found in Appendix B. This system comprises a hall effect sensor, which is mounted on a bracket attached to the frame, and a magnet fixed to the end of the pendulum axle. This configuration is detailed in Figure 3.5. This digital approach offers significant advantages, it provides a constant readout of the pendulum's current position and allows us to gather more comprehensive data on the impact, including velocity and acceleration.

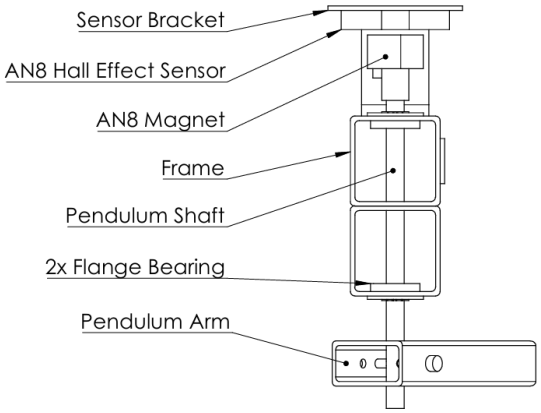

Figure 3.5: Detail of the pendulum shaft, with the AN8 Hall effect sensor mounted to it.

The electromagnetic sensor operates with a 5 V input and outputs a voltage as a percentage of this input, ranging from 10 % to 90 %. This output voltage is directly proportional to the rotational position of the magnet relative to the sensor.

To record these measurements, the sensor is connected to a computer via an Arduino. The wiring schematic is straight forward, with the sensor requiring only a 5 V, analogue in, and ground connection. On the computer, MATLAB is utilized to provide a live feed from the sensor and to control the start and end of data recording. The corresponding MATLAB code can be found in Appendix E.

The measurement system is calibrated so that the pendulum's vertical top point corresponds to 0 degrees rotation, and the impact point is at 180 degrees. The primary goal of these measurements is to determine the difference in potential energy before and after impact.

The initial potential energy is calculated based on the pendulum's starting position, its measured weight, and the gravitational constant. Similarly, the final potential energy is determined using the pendulum's weight, the gravitational constant, and the highest point reached by the pendulum after the first impact.

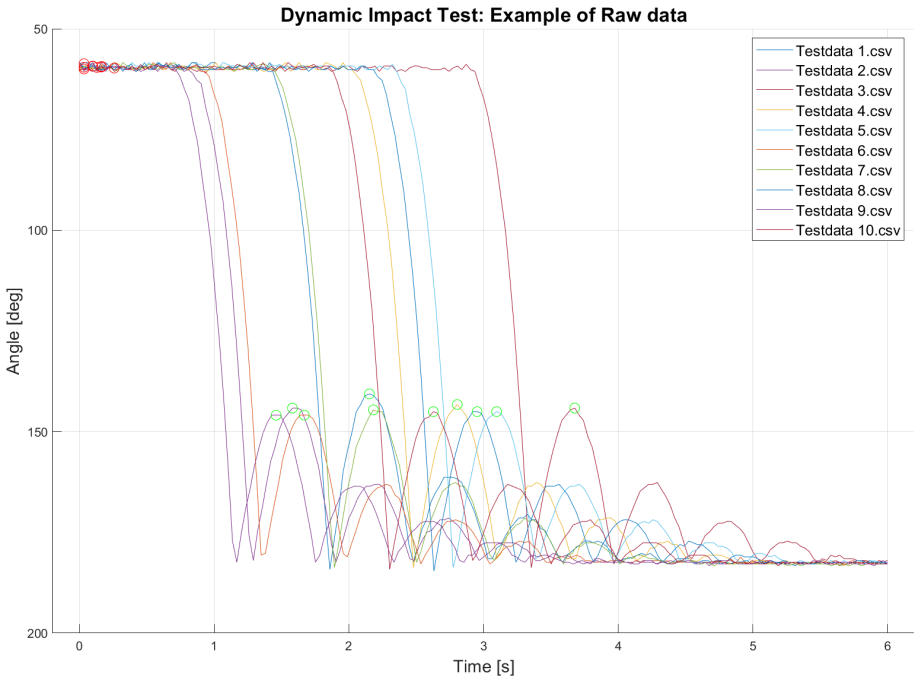

Figure 3.6: Example of data collected by the measurement system. The red and green markers indicate the initial value and the first peak value, respectively.

To accurately calculate these potential energies, the pendulum arm's properties are first determined. This involves measuring its total weight and then identifying its centre of mass. The centre of mass is determined using a simplified two-point measurement method, based on the approach described by Zhang et al. (2019). This centre of mass is used to get the correct height used in the potential energy formula. Once both the initial and final potential energies are obtained, the energy dissipation can be calculated as the percentage loss of this potential energy. The code used for analysing these measurements is provided in Appendix G. An example of the measured data and a visualization of its analysis can be seen in Figure 3.6.

3.5 Discussion

The resulting test setup successfully allows for the measurement of energy absorbing characteristics of mechanical metamaterials. The final design is shown in Figure 3.7. While this design provides a solid, easily reproducible design, several areas could be improved for enhanced performance and precision.

Figure 3.7: Pictured is the dynamic tester with a sample mounted and ready for testing. Table clamps were used to prevent the tester from moving due to the impact force.

The current design could be improved by adding additional stiffeners to better counteract the out-of-plane forces created by the pendulum. While the existing stiffener placement maximizes their effectiveness in enhancing stiffness along the working directions of the pendulum and impact, a slight rotation of the vertical pole structure remains possible when forces are applied in unintended directions. Eliminating these instabilities would be beneficial, as it would remove uncertainties regarding their influence on the testing results.

Manufacturing tolerances could be significantly improved by using solid blocks of steel at connection points instead of pipe steel. Drilling precisely aligned holes through pipe steel proved challenging, with the only critical alignment point, the holes for the pendulum axle, having a slight misalignment of $\ll 0.1$ mm. Employing solid steel blocks would inherently allow for much tighter tolerances. Furthermore, engaging a more experienced craftsman for manufacturing would enhance the overall precision of the setup, as current welding and sawing processes introduced minor deformations that reduced accuracy.

The sample holder size is currently design around the test samples tested in chapter 4. The Charpy impact test has a standardized sample size, standardization is something that needs to be introduced to be able to compare the different samples across a standardized test. Which can enhance the comparison between different research data.

The accuracy of the current measurement system is primarily constrained by the resolution of both the sensor and the Arduino used for data acquisition. The sensor has a specified accuracy of ± 12.6 degrees, while the Arduino's analogue-to-digital converter further limits precision by discretizing the input signal into 1024 steps, introducing an additional quantization error of approximately ± 1.8 degrees. Combined, these limitations yield a theoretical Root Mean Squared Error (RMSE) of approximately ± 9 deg for the complete measurement system.

Although this estimated RMSE appears relatively high, the actual observed measurement error was significantly lower, with deviations being estimated at being less than ± 5 degrees. Moreover, repeated measurements helped mitigate the impact of random error, thereby reducing its influence on the final results.

To improve the accuracy of future impact tests, reducing this combined measurement error is needed. This could be achieved by selecting a sensor with higher inherent accuracy and pairing it with a data acquisition system that provides higher resolution than the current Arduino analogue output.

The new testing method offers significant improvements over existing methods found in literature. It can measure the energy absorbing capabilities of various mechanical metamaterials while using a simpler construction. Simultaneously, it increases precision and simplifies data collection, especially when compared to methods relying on video analysis.

By properly defining the maximum forces as a baseline, the testing setup's structure performed as desired, exhibiting no noticeable deformations even after extensive impact testing. Furthermore, the adjustability of both the hammer's impact force and its impact surface makes this platform as a highly suitable tool for further research within the field of energy-absorbing materials.

3.6 Conclusion

This chapter details the design and development of a new dynamic impact tester, inspired by the working principles of the Charpy impact test, but with the change of it being designed for the use of testing energy absorbing materials. By addressing limitations of existing methods, this method provides a superior balance of simplicity, precision and ease of use.

Key to this approach are the reduced impact forces, and using an improved measuring method than those used in the original Charpy impact test. Using a digital rotation sensor, this design provides comprehensive insights into the impact hammers full motion, making it useful for measuring the energy absorption characteristics of material samples.

The structure itself prioritizes simplicity, utilizing square pipe steel to minimize both cost and complexity. Besides the simple construction, the design offers room for flexibility. This allows for various modifications: by changing the impact force of the pendulum, the energy absorption of materials with a higher toughness can be measured; the impact surface can be swapped, to for example a point force, for different impact scenarios; and the sample holder can be altered, to be able to handle different geometries used in future research.

While the current setup successfully demonstrates its intended functionality, several areas for future improvements have been identified. These primarily concern manufacturing tolerances, the need for improved craftsmanship, and an upgrade to the measuring hardware. Despite these potential improvements, this platform presets a robust and versatile design. Its ability to measure energy absorption with a simpler design and improved data collection methodology, positions it as a valuable tool for advancing the field of energy absorbing materials.

Chapter 4

Energy absorbing metamaterials

4.1 Introduction

Following the literature review in chapter 2, a standardized design was developed based on widely used bistable triangle flexures, known for their wide range of energy absorption capabilities. This design is parameterized and can be adjusted through geometric parameters. With this standardized design, a set of samples were produced where the angle and thickness of the flexure was altered. These parameters are systematically varied to examine their influence on the sample's energy absorbing performance. The primary goal of this study is to identify and understand the relationships between these design parameters and the corresponding energy absorption characteristics.

The analysis is carried out through the fabrication and testing of multiple samples made from TPU. The samples, are tested using two experimental methods. First, a quasi static test is performed using a Tensile testing machine. Subsequently, dynamic impact testing is conducted using the setup and methodology described in chapter 3, allowing evaluation of performance under dynamic impact forces.

Finally, the collected testing data is analysed to identify trends in energy absorption behaviour across the different design parameters. This includes comparing force displacement responses, calculating dissipated energies, and observing the structural deformation. The results aim to provide insight into how the angle and thickness design parameters can be optimized to enhance the energy absorbing capabilities of bistable mechanical metamaterials.

4.2 Method

Following the review of literature, key trends in the design of energy absorbing metamaterials have been identified. Based on these insights, the decision was made to focus on the design parameters of bistable triangle flexures, as illustrated in Figure 4.1. This section outlines the design and testing methodology for these flexures, with the aim of finding a relationship between their energy absorbing capabilities and specific geometric parameters.

4.2.1 Meta Material design

The various designs found in the literature can be broadly categorized into two stacking methods and four distinct flexure types. An illustration of these flexure types is shown in Figure 4.1. The four flexure types are defined based on geometry and configuration:

- **Straight Flexures:** These are the simplest type, consisting of a straight connection between structural nodes.
- **Curved Flexures:** These incorporate a predefined curvature, which dictates the preferred bending direction during deformation.
- **Double Straight Flexures:** Same as the Straight flexures, but two flexures are used per side.
- **Double Curved Flexures:** Same as the Curved flexures, but two flexures are used per side.

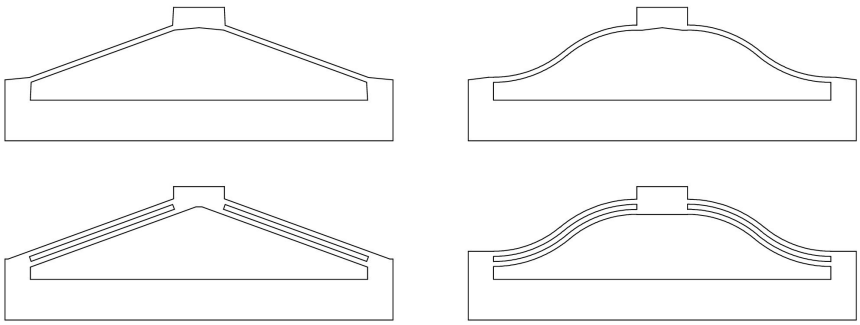

Figure 4.1: This figure shows the different flexure types commonly used in literature.

Stacking Methods Triangle flexures can be arranged using several stacking patterns. The first method uses a staggered grid, where the base unit is repeated uniformly along both the x - and y-axes. The second method applies a bricklaying-style tessellation, in which each row is offset by half the unit width relative to the row below, creating a staggered, interlocking pattern.

The third and fourth configurations are variations of the first two, where the triangle orientation is flipped in alternating rows. This results in the same overall tiling pattern as the original two, without introducing a new structural layout. As such, these four configurations yield two distinct stacking approaches in terms of geometry and load distribution. The different stacking patterns are illustrated in Figure 4.2.

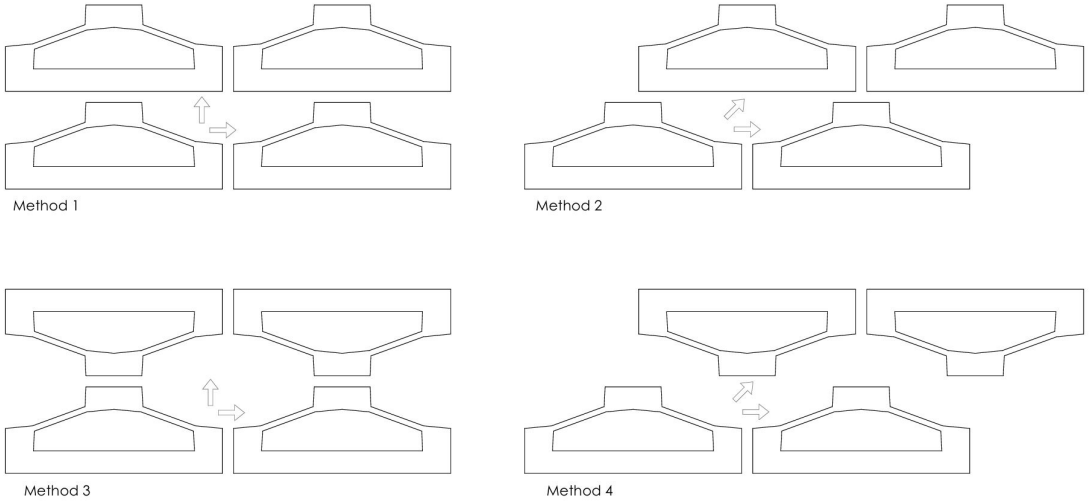

Figure 4.2: Overview of different stacking patterns.

For this study, the tested designs were limited to the staggered grid stacking pattern, combined with the single flexure variants of both the curved and straight configurations.

Parameters of the Flexure

To generate the different test samples, two parameterized models were developed: one for the straight flexures and one for the curved flexures. The construction of both configurations is illustrated in Figure 4.3. The remainder of this section provides a detailed description of each design parameters used in the construction of the metamaterial.

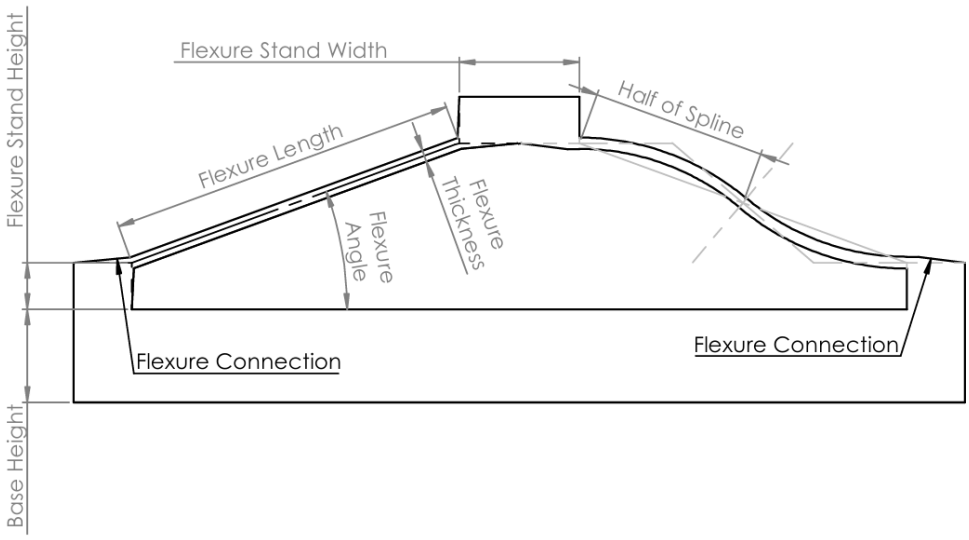

Figure 4.3: Overview of the parameters used in the construction of both the straight and the curved flexure.

Flexure Angle The flexure angle is one of the most impactful design parameters, as it significantly influences the overall height and width of the metamaterial. The angle is defined from the positive x-axis to the positive y-axis and is measured at the connection points on the support stands. Based on the findings from the literature review (chapter 2), there appears to be a positive correlation between the flexure angle and the energy absorbing capability, with steeper angles generally leading to increased energy dissipation.

Flexure Length The flexure length is the second most influential parameter in the design of bistable triangle flexures. It has a strong impact on the bistable behaviour of the structure, particularly affecting the range and nature of its stable states. This parameter, in combination with the flexure thickness, defines the overall mechanical response of the flexure, when not considering the angle. The flexure length is measured between the two connecting stands, as illustrated in Figure 4.3. In addition to its influence on mechanical performance, this parameter also significantly affects the overall height and width of the metamaterial.

Flexure Thickness Flexure thickness has a significant impact on the stiffness and bistability of the flexures. It alters the material's resistance to bending and thus affects how easily the structure transitions between its stable states. Small variations in this parameter can lead to noticeable changes in the energy absorption capabilities of the metamaterial. The Flexure thickness is defined around the hearth line of the connection line between the two stands.

Unit Thickness The unit thickness refers to the out-of-plane thickness of the metamaterial. Although it does not significantly affect the bistable mechanical behaviour of the design, it linearly scales the total force and energy required during deformation. This parameter becomes particularly important when considering practical applications and use cases, as it directly impacts the load capacity and overall energy absorption potential.

Straight or Curved flexure While the straight flexure is defined as a linear connection between the two stands, the curved flexure consists of a spline composed of two symmetrical curves that meet at the midpoint of the gap between the stands. These curves are designed to be collinear at the midpoint, forming a smooth S-curve. At both ends, the spline is tangent to the horizontal top surfaces of the stands. An example of this geometry can be found in Figure 4.3.

Stand and Base Height, and Stand Width The stand height, base height, and stand width are the final parameters needed to fully define the bistable triangle flexure design. The stand height ensures sufficient clearance for the flexures to fully fold into their bistable positions. The stand width contributes to the overall stiffness at the attachment points, providing stable boundary conditions for the flexures. Similarly, the base height enhances the stiffness between the stand's attachment points of the flexure triangles, further supporting stable boundary conditions.

Unit Height and Width The overall height and width of the bistable triangle flexure units are not predefined, but are instead determined by the above defined design parameters, particularly the flexure angle and length. As such, these dimensions are design-driven and adapt dynamically with changes of the input parameters.

Flexure Connection The flexure connection refers to the additional material used to connect the flexures to the stands. This feature is only necessary at extreme flexure angles, where the standard connection geometry may no longer provide sufficient strength. The connection is not explicitly parameterized, instead it is derived from the existing geometry of the stand and the flexure. An example of this connection is shown in Figure 4.3.

4.2.2 Material Selection

To fabricate test samples, a material selection was conducted based on the following criteria: ease of manufacturing, high flexibility, and availability.

Plastics offer a wide range of mechanical properties and are generally well suited for rapid prototyping. Materials such as PLA and ABS were initially considered due to their ease of printing and wide availability. However, their high stiffness and yield strength rendered them unsuitable for the flexible deformation required in bistable flexures. Initial test samples produced from these materials reached their fatigue limits after limited cycles, leading to early mechanical failure.

In contrast, rubber-like materials such as TPU emerged as the most promising option, offering the necessary flexibility and elasticity to endure repeated cycles of compression and extension without mechanical failure. Ultimately, TPU A95 HF from Bambu Lab was selected, as it was suitable and readily available in the manufacturing workshop. The corresponding material specifications can be found in Appendix C.

Manufacturing Method Several fabrication methods were evaluated. Casting using Moulds was ruled out due to the impracticality of producing a new mould for each design variant, a mould which can be adjusted to the right parameters was also too complex. Laser cutting and water jetting of TPU sheets were also explored but lacked the required precision on the available equipment.

Ultimately, Fused Deposition Modelling (FDM) 3D printing was selected as the most viable manufacturing method. It offered high flexibility in design variability, good accuracy, and accessibility. All test samples were therefore produced using FDM with TPU A95 HF filament.

4.2.3 Testing series

This study focuses on single flexure, both straight and curved, combined with the staggered stacking pattern. The primary design parameters under investigation are the flexure angle and flexure thickness.The tested samples are categorized into three groups, series A1, A2, and B.

Series A1 consists of straight bistable flexures with varying flexure angles, while Series A2 contains curved bistable flexures with the same variation in angles. For both series, the initial design range covered angles from 10 to 80 degrees, manufactured in five steps, with the objective of investigating the relationship between flexure angle and energy absorption capability.

The first set of samples was fabricated using Black TPU A95 HF by Bambu Labs (Appendix C). However, the sample with an 80 degree angle exhibited significant shearing and deviation from the intended compression axis, rendering it untestable. As a result, the maximum testable angle in subsequent sets was limited to 62.5 degrees.

Following promising results from the initial series, three additional samples were added at intermediate angles to refine the resolution of the data. These samples were produced using Blue TPU A95 HF from the same manufacturer. Due to noticeable differences in mechanical behaviour between the black and blue filament variants, the original samples from series A1 and A2 were also reproduced in Blue TPU to ensure consistent material properties across the dataset. For both A1 and A2, the flexure thickness was fixed at 1.5 mm throughout all tests.

Series B focuses on straight bistable flexures with a constant flexure angle of 27.5 degrees, while varying the flexure thickness. The thickness of the flexure ranges from 0.6 mm to 2.4 mm, in increments of 0.3 mm. This series investigates the influence of flexure thickness on the energy absorption characteristics. All other design parameters are kept consistent with Series A1 and A2.

A detailed technical drawing of the sample design is provided in Figure 4.3, and a complete list of all sample dimensions is included in Appendix D.

4.2.4 Testing Methodology

Sample specification Due to the impracticality of producing and testing all possible combinations of the design parameters, selected design series were defined. Each series first undergoes quasi-static testing, followed by dynamic impact testing.

Samples are fabricated using Fused Deposition Modeling (FDM) printing with TPU A95 HF filament (Appendix C), printed on a Bambu Lab X1 series printer. The standard slicing settings are used, with a layer height of 0.20 mm and a 0.4 mm nozzle. To maximize stiffness, the infill is configured as a grid pattern with 100 % infill density, ensuring that deformation is concentrated in the flexure regions rather than the structural elements. All other print settings remain at their default values. Post-processing is minimal, consisting only of the removal of minor stringing or webbing, common with printing TPU, using flush cutters.

Each sample includes an additional 6mm diameter hole for inserting a metal rod. This design modification was implemented following initial quasi static tests, which revealed undesired deformation at the base of the sample due to the limited clamping width of the tensile testers fixture. The inserted rod increases stiffness in the base region, ensuring a more uniform distribution of forces across the sample during testing. The CAD model of the modified sample is shown in Figure 4.4, and a photo of the quasi static test setup is provided in Figure 4.5.

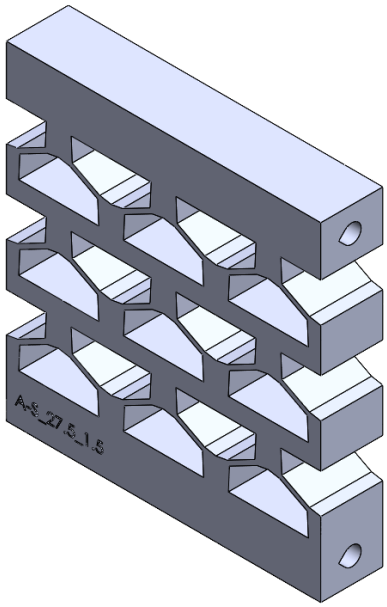

Figure 4.4: CAD model of a straight flexure sample, with an angle of 27.5 degrees and a thickness of 1.5 mm.

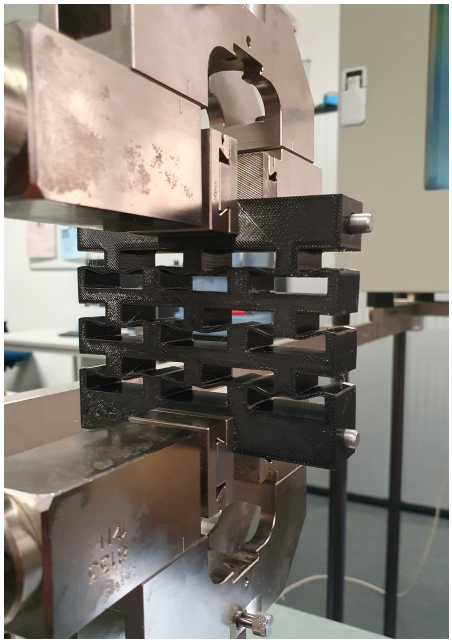

Figure 4.5: Sample mounted in the Tensile test setup, for measuring the quasi static behaviour.

Quasi static testing The quasi static test procedure is as follows, the total travel distance for compression and decompression is defined by the vertical distance between the support stands. This is then multiplied by layers in the tested sample. Each sample undergoes a full initial cycle, to give the sample its first full deformation. This is followed by five repeated cycles to evaluate both energy dissipation performance, and the multiple cycles also give insight in the material's fatigue behaviour. The data provided by the quasi static testing setup, is the force displacement curve of the sample, this data is then exported to be processed in MATLAB.

In MATLAB, the area under the force-displacement curve is calculated separately for each compression and decompression phase. The difference between the compression and decompression phase gives an approximation of the dissipated energy. This is repeated for all five cycles, and across all the samples. Finally, the resulting energy dissipation is plotted as a scatter plot, and trend lines are created to analyse the relationship with the design parameter of interest. The corresponding MATLAB code can be found in Appendix F.

Dynamic testing For the dynamic test, each sample is mounted in the testing setup described in chapter 3. The holder frame is positioned such that the lowest point of the pendulum swing aligns precisely with the top surface of the sample. The sample is then clamped at the appropriate height, completing the setup for dynamic testing. Each sample undergoes testing at four different impact energy levels, with ten repetitions per energy level to ensure reliable performance data.

During each test, the angular position of the pendulum is recorded. Specifically, the initial release angle and the return angle after the first impact are of interest. These two measurements are used to calculate the energy dissipated by the sample, by using the difference in potential energy between the two positions. The recorded data is then processed in MATLAB, where the dissipated energy values are computed and visualized in scatter plots with added trend lines to visualize correlations. The corresponding MATLAB code can be found in Appendix G.

4.3 Results

4.3.1 Dogbone Test

To characterize the material properties of the test samples, three tensile test specimens were produced and tested according to the ISO 527-1 standard. This characterization was performed twice, for both the black and blue variant of TPU A95 HF from Bambu Labs, due to the notable difference in tactile feel and observed mechanical behaviour during the tensile testing.

As shown in Figure 4.6, the two batches exhibited significantly different stress–strain responses. The projected yield strength differed by more than 20 % between the black and blue TPU variants. Additionally, both materials showed Young's moduli that were approximately four times higher than the values reported in the manufacturer's datasheet (Appendix C), with a relative difference of around 40 % between them. These discrepancies limit the direct comparability of results between the black and blue sample sets and highlight the importance of consistent material sourcing for experimental repeatability.

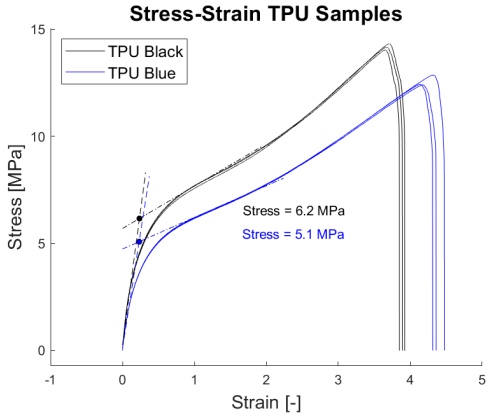

Figure 4.6: ISO 527-1 dog bone test of the black and blue TPU, while the specification should have yielded similar results, this is clearly not true, the difference in performance is approximately 20 %. The corresponding Young's moduli are 50 MPa for black and 34 MPa for blue.

4.3.2 Quasi static test results

The quasi static tests were conducted in three sessions. Each sample was subjected to a single repetition followed by a set of five repeated cycles. An example of the measured data is shown in Figure 4.7, where a slight difference can be observed between the responses of the black and blue TPU samples.

In addition to material differences, the flexure angle had a strong influence on mechanical behaviour. Higher-angle samples exhibited more pronounced non-linear responses, with the largest angles displaying signs of negative stiffness behaviour. As the angle increased, the tensile tester required a higher force to achieve compression of the sample. Although all samples ultimately reached a fully compressed state, the higher-angle specimens showed slight out-of-axis buckling. This instability is evident in the irregularities present in the force displacement curve of the 62.5 degree sample.

The samples with an 80 degree flexure angle could not be fully compressed during testing due

to significant sideways buckling, which prevented axial compression. Images of the quasi static testing setup and resulting out of axis deformations can be found in Figure 4.8.

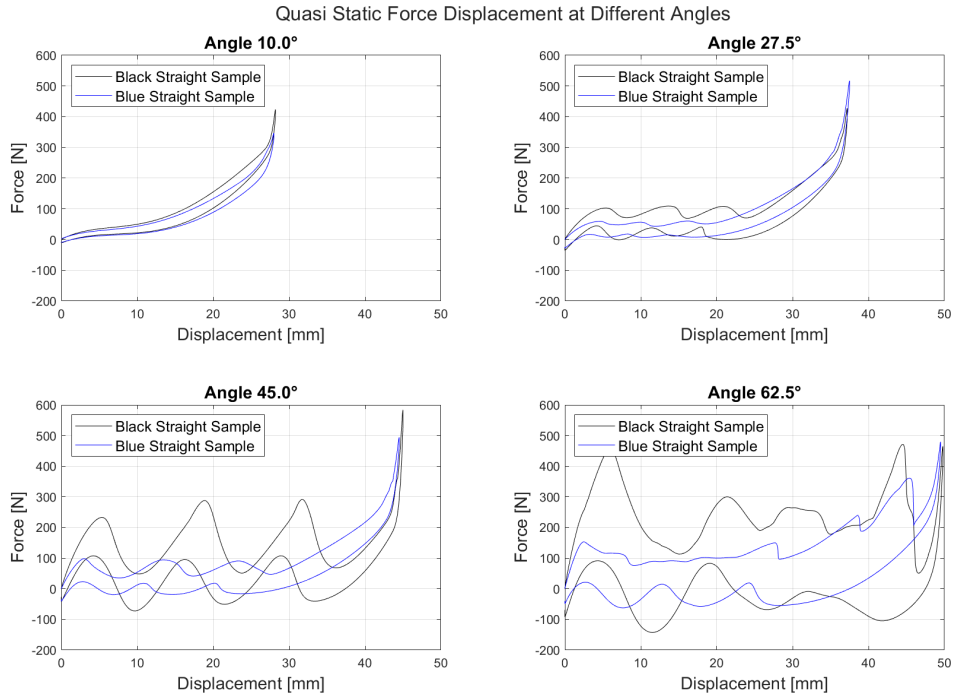

Figure 4.7: The raw force displacement data from the quasi static tests for both the black and blue TPU samples. These results indicate that negative stiffness behaviour is observed only in samples with high flexure angles, while lower-angle samples exhibit more linear or monotonic responses.

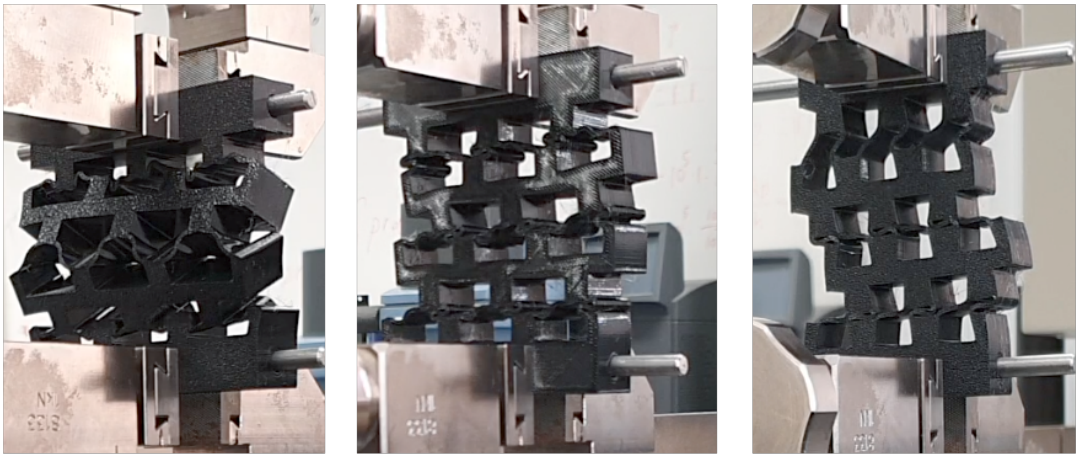

(a) **(b)** **(c)**

Figure 4.8: a) Sample exhibiting slight out-of-plane buckling, this sample was able to fold into the fully compressed state. b) Sample showing mild side buckling, which still allowed full compression. c) Sample with significant side buckling, preventing it from reaching full compression.

The measured force displacement data were converted to corresponding energy dissipation values. Figure 4.9 illustrates the performance differences between the black and blue TPU samples. Note that the black TPU series includes fewer data points due to the mid-study transition to the blue TPU material. The results show that the black TPU samples consistently exhibit higher energy dissipation coefficients compared to the blue TPU, indicating a significant material dependent influence on the energy absorption performance.

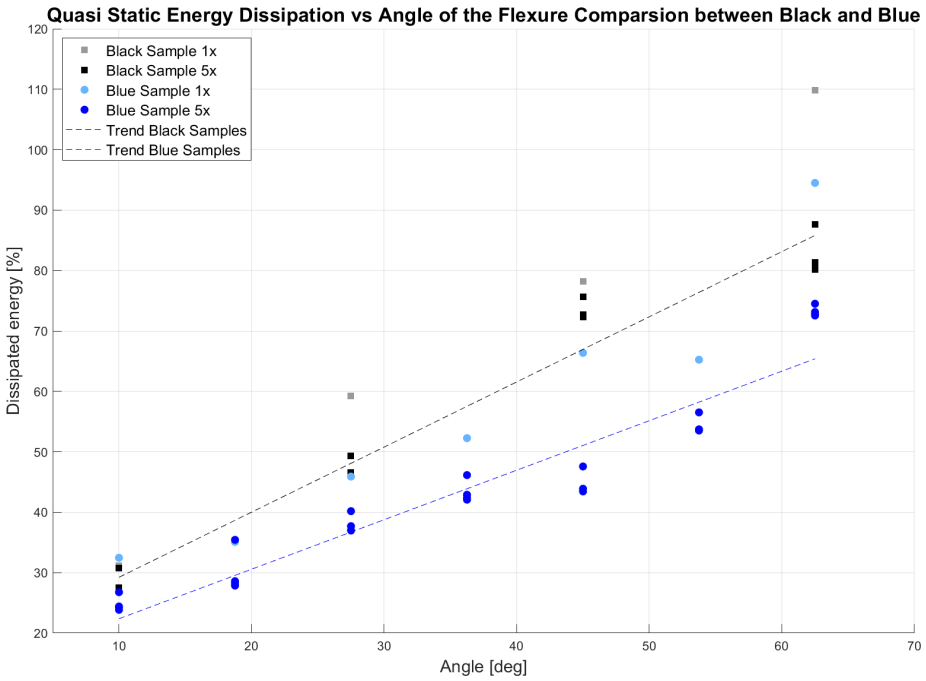

Figure 4.9: This figure shows the difference between the energy dissipation of the quasi static test between the blue and the black TPU samples.

Next, a comparison between the straight and curved flexure designs was made. In Figure 4.10, the energy dissipation is plotted as a function of the flexure angle for both the straight and curved series. The curved flexures show higher energy dissipation values, with some exceeding 100 %. The straight flexures display a clearer and more consistent trend in energy dissipation across the tested angle range.

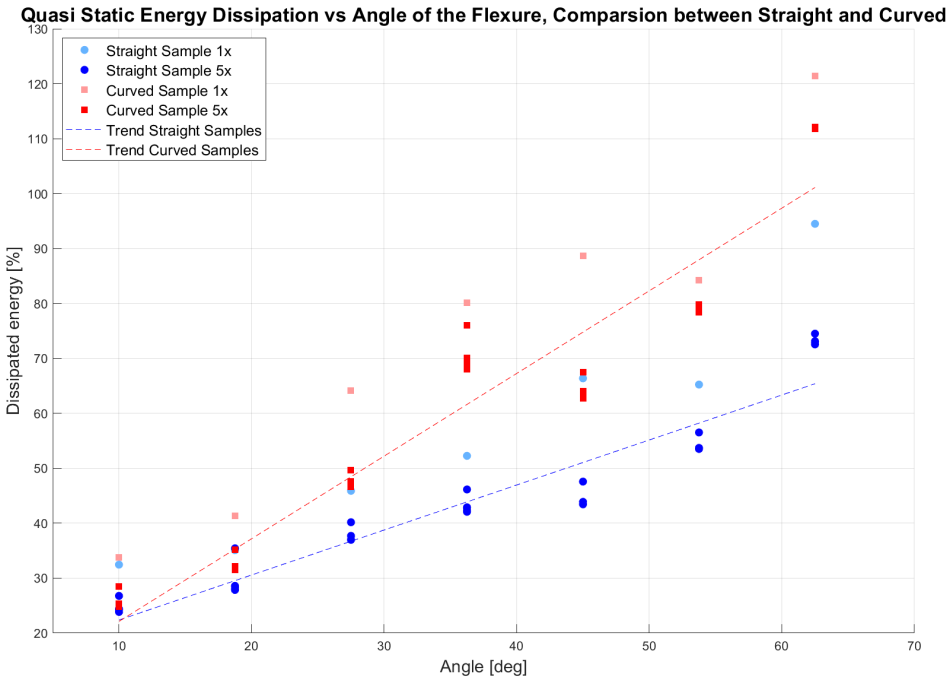

Figure 4.10: This figure shows the difference between the energy dissipation numbers of the quasi static test between the straight and curved samples.

Finally, the energy absorption results for the second series, which varies the flexure thickness, are presented in Figure 4.11. This data is based solely on the blue TPU samples, with thickness ranging from 0.6 to 2.4 mm with increments of 0.3 mm. The results indicate that energy absorption appears to be largely independent of flexure thickness within the tested range.

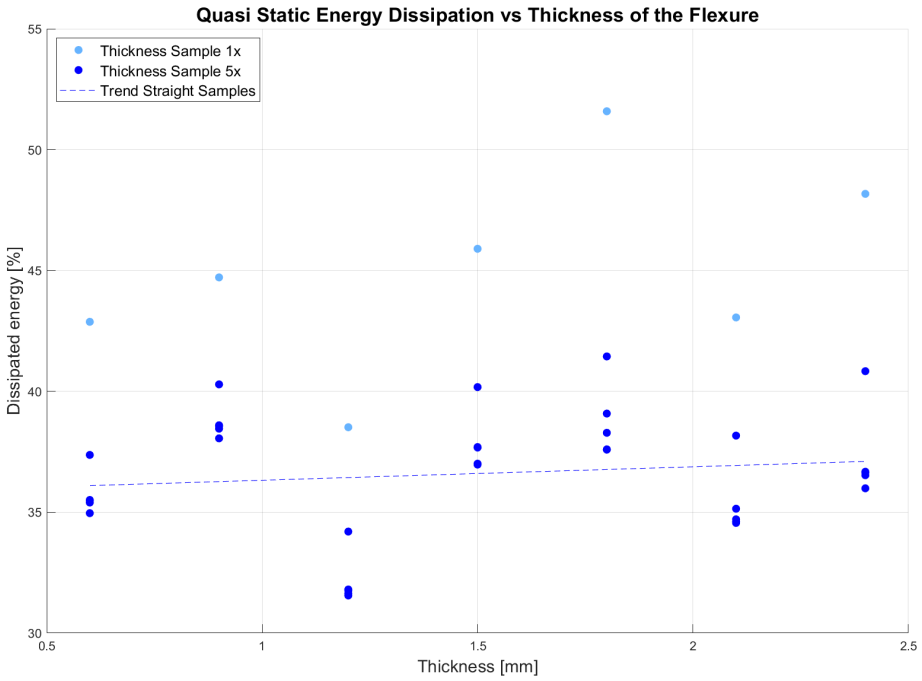

Figure 4.11: The quasi static measured energy dissipation of samples with varying thickness.

For all tested samples, the initial single-cycle test consistently exhibits significantly higher energy dissipation compared to subsequent repeated cycles, indicating the presence of viscoelastic behaviour.

4.3.3 Dynamic test results

For the dynamic tests, the same samples used in the quasi static testing were used, with each sample tested 10 times in quick succession. The applied impact energy on the samples was varied to match the difference in required compression forces observed in the quasi static testing.

For the figures presenting the frames captured during the impact (Figure 4.14, Figure 4.16 and Figure 4.19), the following describes the timing of each frame: Frame 1 shows the moment at or just before impact. Frame 2 captures the hammer halfway through the impact. Frame 3 corresponds to the point of full compression. Frame 4 shows the halfway point during the extension phase. Frame 5 captures the moment when the hammer passes the initial contact point again. Frame 6 shows the hammer after it has moved beyond the original impact position. Finally, Frame 7 captures the flexures when the hammer reaches its highest point, at which the flexures show the condition they will end in.

Starting again with a comparison between the Black TPU and Blue TPU series, the resulting characteristics are shown in Figure 4.12. For these tests, the pendulum weight was set to an impact energy of 0.4 J. A significant difference in dissipated energy between the two materials

is evident. Additionally, the observed trend lines differ notably from the quasi static test results, exhibiting a second-order relation. The absolute values of the dissipated energy are also significantly higher in the dynamic tests compared to the quasi static tests.

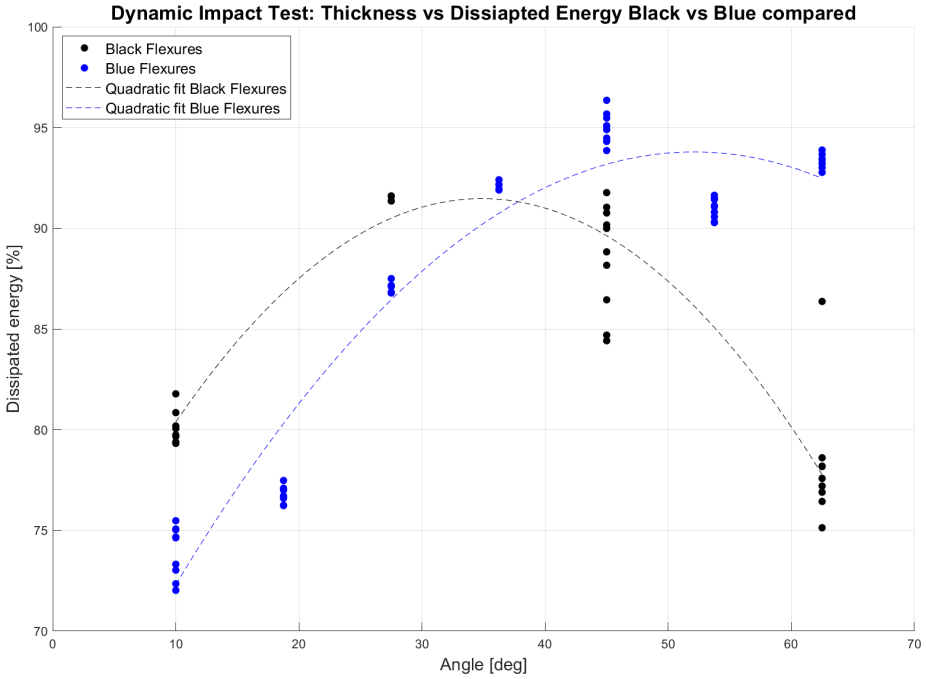

Figure 4.12: This plot shows the dynamic test results of the blue and black samples with different angles, subjected to an impact energy of 0.4 J.

The resulting characteristics of series A1 and A2, representing straight and curved samples with varying flexure angles, are shown in Figure 4.13 and Figure 4.15, respectively. The straight samples exhibit a maximum dissipated energy at the 0.4 J impact energy, with the trend transitioning toward near-linear behaviour as the impact energy increases. Interestingly, higher impact energy appear to inversely affect energy dissipation for samples with large flexure angles, while at lower angles, the dissipation remains relatively constant between the different impact energies. In contrast, all curved samples consistently show a peak in energy dissipation with respect to the flexure angle. It is also evident that increasing the impact energy shifts the angle at which maximum energy dissipation occurs.

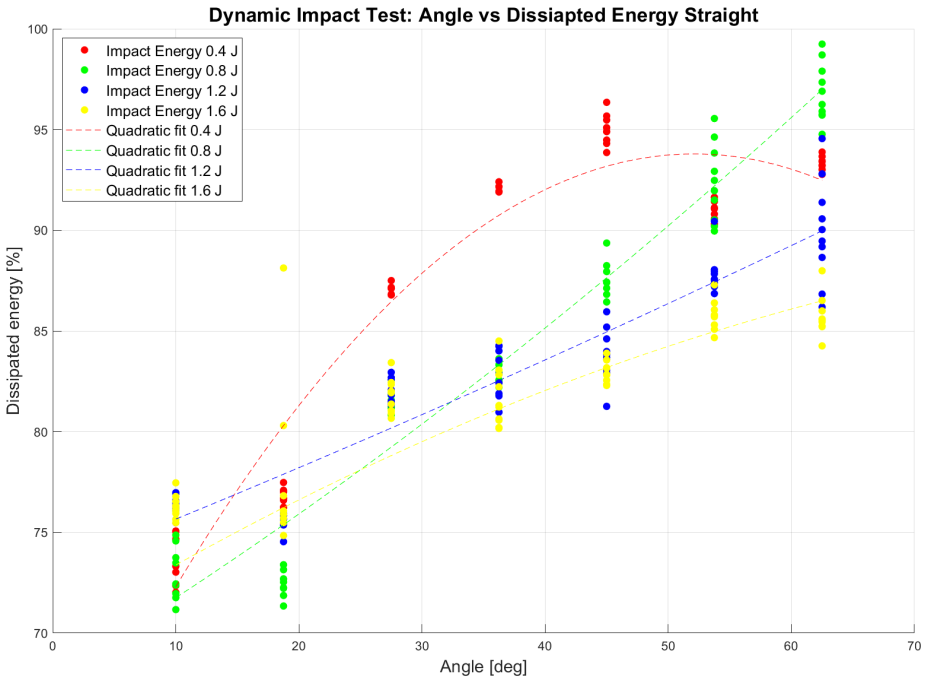

Figure 4.13: This figure illustrates the energy dissipation of straight samples with different angles, subjected to four different impact energies.

To highlight these differences, a comparison between straight and curved samples is presented in Figure 4.17, where the quadratic behaviour of the curved samples contrasts with the more linear trend of the straight samples. For a set of samples, a slow motion video was taken, this can be seen in Figure 4.14, for the straight samples and in Figure 4.16 for the curved samples. It can be seen that the behaviour is different for each sample, where the response is homogenous for the samples at 10 degrees angle, at 45 degrees a layered response can be observed. The Straight flexure at 62.50 degrees, and the curved sample of 45 degrees, remained folded after impact. The Curved sample of 62.50 did not fully compress during the dynamic tests.

For series B, the samples exhibited behaviour similar to that observed in the quasi static tests. As shown in Figure 4.18, the energy dissipation remains relatively constant across the range of thicknesses tested. Interestingly, the energy dissipation is lowest at the 0.8 J impact force level, while the lower and higher impact energies yielded higher dissipation values. A slight downward trend in energy dissipation with increasing thickness is noted in the dynamic tests, which contrasts somewhat with the flat trend observed in the quasi static testing results, but this difference is not significant. Also for the thickness variation test photos of the dynamic impact were taken, this can be seen in Figure 4.19. Here it can be seen that for all thicknesses the response is similar.

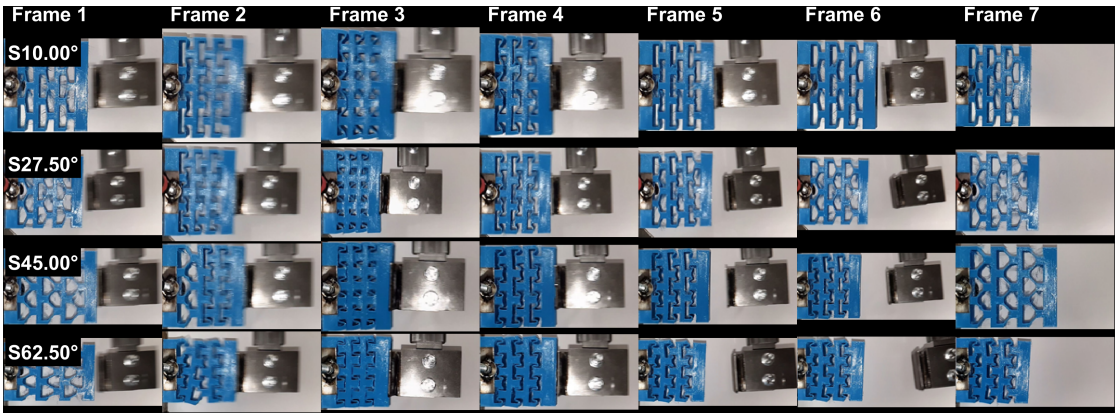

Figure 4.14: This figure presents frames capturing the impact on various straight samples subjected to 1.2 J of impact energy.

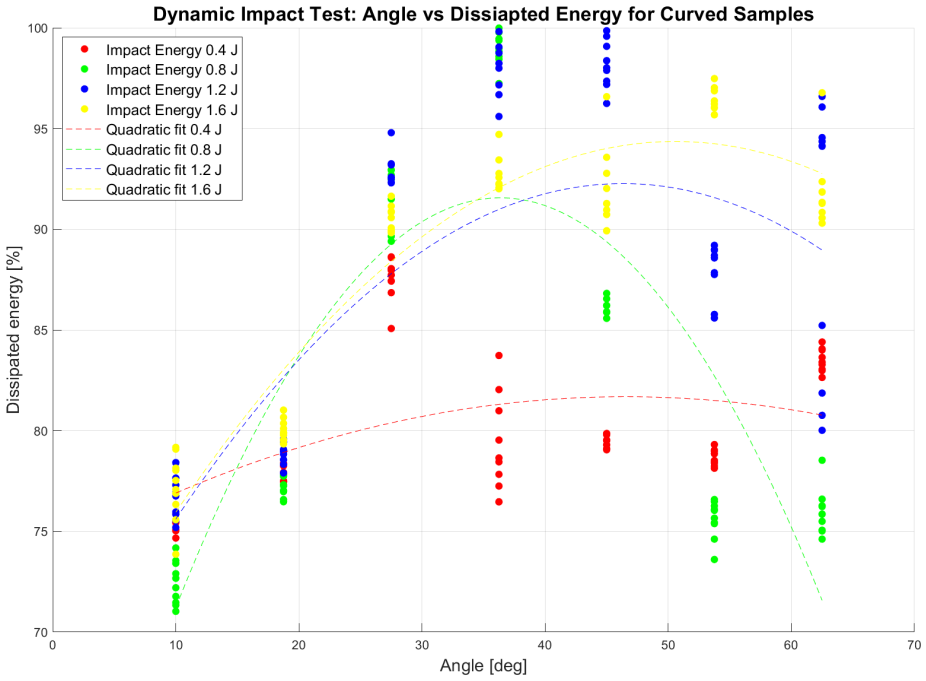

Figure 4.15: This figure illustrates the energy dissipation of curved samples with different angles subjected to four different impact energies.

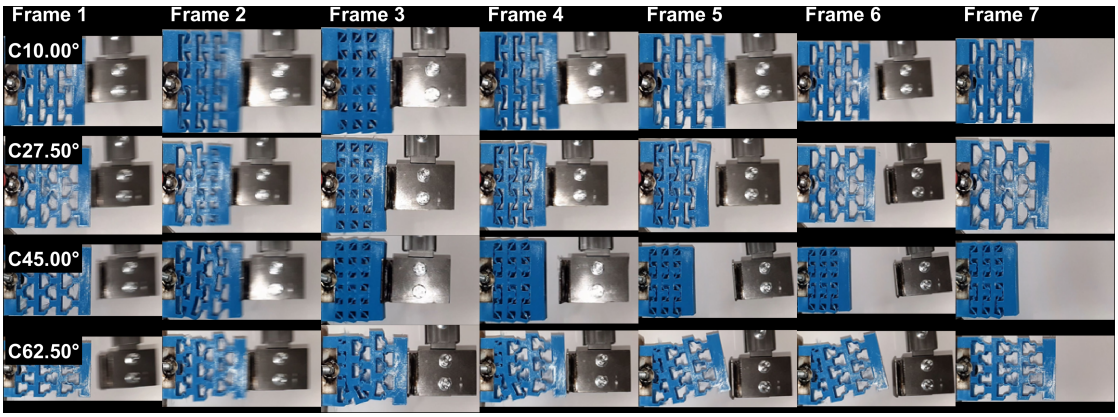

Figure 4.16: This figure presents frames capturing the impact on various curved samples subjected to 1.2 J of impact energy.

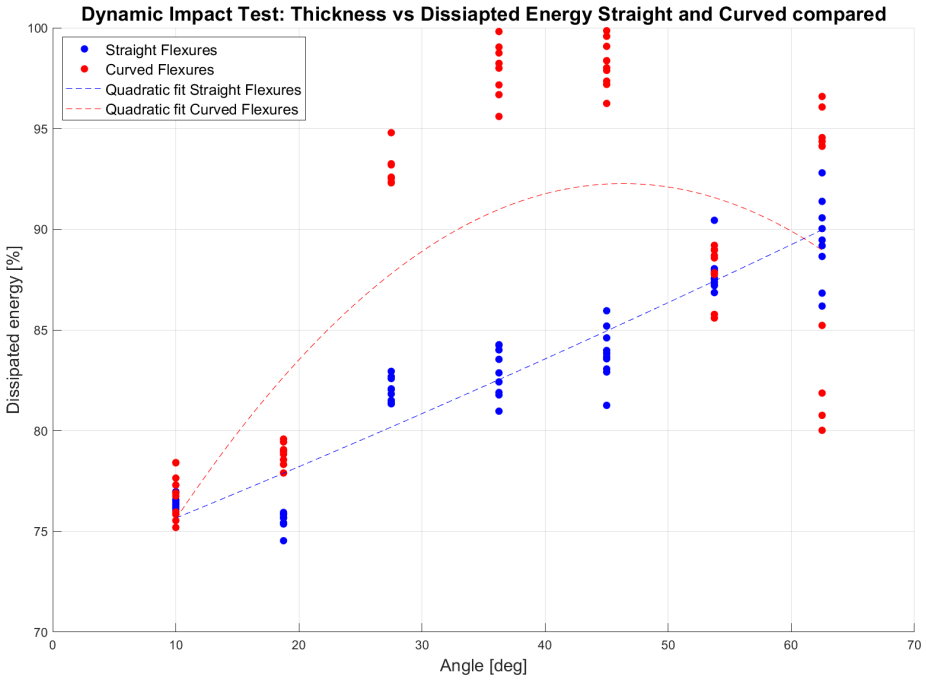

Figure 4.17: This figure shows a comparison between the straight and curved samples at a dynamic impact of 1.2 J.

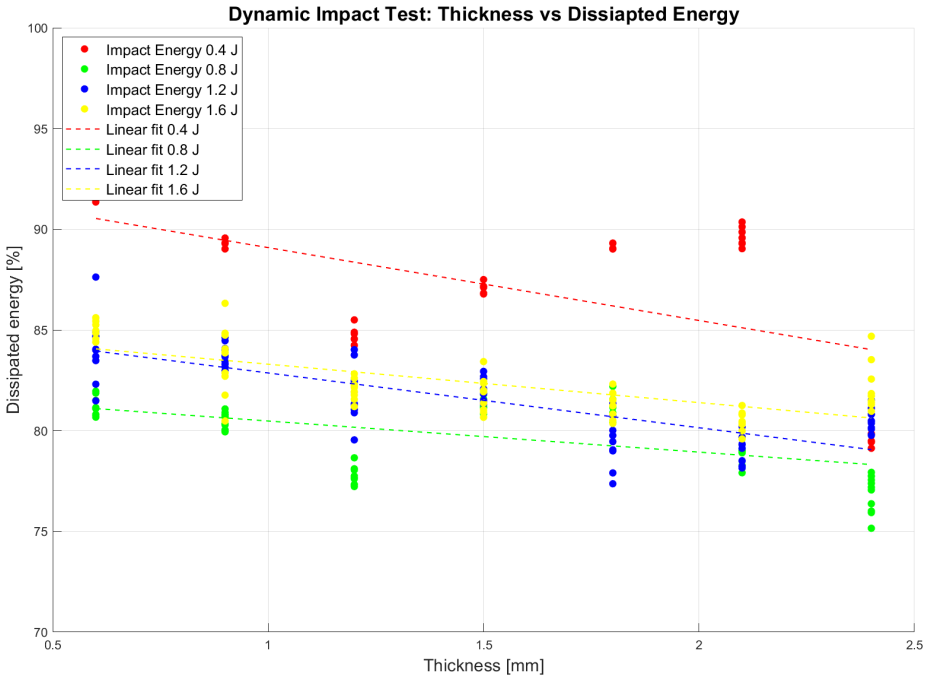

Figure 4.18: This figure illustrates the energy dissipation of straight samples with different thicknesses, with a fixed angle of 27.5 degrees, subjected to four different impact energies.

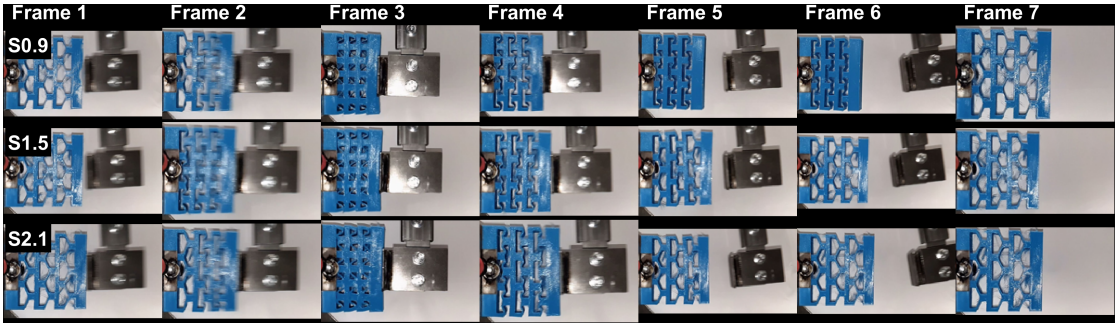

Figure 4.19: This figure presents frames capturing the impact on various straight samples with varying thicknesses, the samples have a fixed angle of 27.5 degrees, and are subjected to an impact energy of 1.2 J.

4.4 Discussion

In this section, the results are analysed and discussed, with a focus on identifying and explaining the observed trends and relationships within the data.

4.4.1 Initial testing

The initial quasi static tests on the black TPU samples revealed significant buckling behaviour in samples with flexure angles greater than or equal to 62.5 degrees, which prevented proper compression. As a result, the samples with an angle of 80 degrees could not be tested. Samples with angles up to 62.5 degrees exhibited some out-of-axis buckling, but were still able to fully compress. This buckling behaviour is most likely due to imperfections in the printed sample and the resulting non-uniform loading in the test setup, causing the sample to deform out of plane. Some of this buckling can be observed in Figure 4.8.

The initial black sample set showed a seemingly positive correlation between flexure angle and energy dissipation in both quasi static and dynamic tests. This trend is visible in Figure 4.7 and Figure 4.9. This relationship held only up to 62.5 degrees. The 80 degrees samples could not be properly evaluated due to severe buckling causing misalignment during testing.

4.4.2 Viscoelastic behaviour in the samples

To account for viscoelastic behaviour during the quasi static tests, each sample underwent an initial preload measurement cycle prior to the full measurement. This step helped stabilise the material response before the full measurement. Following the preload, each sample was subjected to five repeated test cycles. By preloading the samples the remaining viscoelastic effects between cycles were minimized. However, the first cycle consistently required a significantly higher deformation force, suggesting some initial viscoelastic settling.

For the dynamic impact tests, the same samples were reused. Full preloading was thus not necessary in this case. However, to minimise the influence of viscoelastic behaviour during repeated impacts, each sample was subjected to one unmeasured impact trial prior to the ten measured repetitions.

4.4.3 Material differences between black and blue TPU

After producing a second batch of samples using Blue TPU A95 HF, it was immediately apparent that the material exhibited less stiffness compared to the original Black TPU A95 HF batch. This was unexpected, as the manufacturer specifies similar mechanical properties for both colour variants.

To investigate this further, additional ISO 527-1 dogbone tensile tests were performed using the blue material. The results, shown in Figure 4.6, confirmed a significant difference. The blue TPU exhibited an approximately 20 % lower estimated yield strength compared to the black TPU samples.

To enable a fair performance comparison between geometries, the original samples were reprinted using the blue TPU material. As shown in Figure 4.9, these new samples demonstrated lower energy dissipation percentages, likely a result of the lower stiffness.

Given the observed differences and the unavailability of the black TPU for continued testing, the decision was made to produce all final samples using the blue TPU. This ensured material consistency across all tested series.

4.4.4 Layered vs non-layered response

During quasi static compression testing, the deformation behaviour varied significantly between samples, depending primarily on the flexure angle. For low angle samples, all three layers deformed simultaneously during the compression stroke, resulting in a uniform force-displacement response. This behaviour is reflected in the data presented in Figure 4.7. The uniformity in deformation is likely due to the absence of negative stiffness in these flexure configurations. Specifically, the force-displacement curves show no regions of negative slope, indicating purely positive stiffness throughout the compression cycle. A visual representation of this simultaneous deformation is provided in Figure 4.14, for the sample with a 10 degree angle.

In contrast, higher angled samples exhibited a sequential, or layered, deformation pattern. This behaviour is characterized by multiple distinct peaks in the force-displacement curves (Figure 4.7), each corresponding to the independent buckling of a specific layer. Typically, the buckling begins with the middle layer, after which either the top or bottom layer buckled, and finally the last layer buckled. During the extension (unloading) phase, the sequence was generally reversed.

The measured data displayed regions of negative stiffness, which was visually represented by the samples snapping into their second stable configuration during deformation. The presence of three distinct peaks is attributed to slight imperfections between the layers, which led to variations in the force required to initiate buckling in each layer. As a result, a consistent sequential deformation order emerged. A visual representation of this layered buckling progression is shown in Figure 4.14 for the sample with a 45 degree angle.

At the highest tested angle of 62.5 degrees, some samples exhibited out-of-axis shearing during compression. This led to buckling, which occasionally caused collisions between the flexure stands, which hindered full compression and resulted in non-uniform deformation behaviour. However, the samples were still able to fully compress. This effect contributed to the deflected force displacement curve in the data observed in Figure 4.7. However, the force-displacement curves remained consistent across all five compression cycles, confirming the repeatability of the behaviour. The observed shearing is attributed to minor manufacturing imperfections inherent to the FDM printing process, which introduce asymmetries and in turn internal stress concentrations. Such imperfections disrupt uniform deformation and are unlikely to be captured in idealized finite element simulations. A visual representation of the shearing behaviour is provided in Figure 4.8.

A similar distinction in deformation behaviour was observed during the dynamic tests. Samples that deformed uniformly under quasi static loading continued to exhibit uniform deformation under dynamic impact. And samples that displayed layered deformation in quasi static testing absorbed energy primarily through the deformation of a single layer at low impact energies. As the impact energy increased, additional layers were sequentially engaged until full deformation was achieved. This layer-wise activation was also consistently observed across repeated dynamic test, indicating that the response is repeatable despite its complexity.

4.4.5 Different impact energies used in the dynamic tests

The initial round of dynamic tests revealed similar behaviour across nearly all samples. The default impact energy was insufficient to fully compress the samples. While low-angle samples exhibited some compression, due to their uniform stiffness response. The hammer tended to bounce off samples with higher flexure angles without causing notable deformation. Based on the quasi static test results, it was estimated that the force required for full compression ranged between 100 N and 400 N. However, the impact energy with the default hammer force was only 0.4 J, which was not sufficient to in reaching high enough compression force for full compression. To address this, additional weights were fabricated and attached to the hammer, increasing the maximum impact force to 1.6 J This adjustment enabled full compression of all but one sample under dynamic loading.

4.4.6 Comparison between dynamic and quasi static tests

The trends observed in the quasi static tests were largely confirmed by the dynamic tests. However, a key difference lies in the range of dissipated energy. In the quasi-static tests, energy dissipation values typically ranged between 40 % and 60 %, whereas in the dynamic tests, dissipation increased significantly, ranging from 70 % to nearly 100 %. This discrepancy can be attributed to the nature of loading in each test.

In quasi static loading, the compression device maintains continuous contact with the sample throughout the entire deformation and recovery cycle. In contrast, dynamic loading involves a short duration, high impact collision from the dropped impacted hammer. After the impact, the hammer often bounces back, and the sample is no longer in contact with the impact source. As a result, a portion of the system's energy remains trapped in the deformed structure and cannot be returned to the hammer, contributing to the higher apparent energy dissipation observed in dynamic tests.

Another phenomenon observed in dynamic tests was sample retained deformation, this is where the sample remained compressed after impact. This behaviour corresponds directly to the force-displacement response from quasi static testing. In cases where the unloading phase dipped below zero, a negative pulling force was required to return the sample to its original shape. Such recovery is feasible in quasi static testing due to the active tensile machine, but impossible in dynamic testing, as the hammer is not mechanically connected to the sample. Therefore, the retained deformation behaviour is only observed during the dynamic testing. The optimal impact energy was found to be between 0.8 J and 1.6 J, depending on the sample.

4.4.7 Relation between angle and energy dissipation in straight flexures

The straight flexures show a clear linear relationship between the flexure angle and the dissipated energy. This trend is consistent across both quasi static and dynamic testing, as shown in Figure 4.10 and Figure 4.13, respectively. In both cases, increasing the flexure angle results in a proportional increase in energy dissipation.

In Figure 4.10, it can be seen that the quasi static force-displacement response for straight flexure samples with increasing angles remains linear across the different angles, with an increasing energy dissipation at higher angles.

Interestingly, results from the dynamic testing show that increasing the impact energy leads to a decrease in dissipated energy for samples with angles above 45 degrees. This is likely due to excess energy in the system, which causes the hammer to bounce back more strongly after impact, resulting in a decreased energy dissipation by the sample. At the lower end of the angle range at 10 and 18.75 degrees, there appears to be little to no difference in energy dissipation across varying impact energies. This is likely because of the linear stiffness response of these low-angle samples, which react similarly regardless of the applied impact energy.

The linear relationship between flexure angle and energy absorption is consistent with findings from the literature review (see chapter 2). The results from Series A1 support this hypothesized behaviour, confirming that higher flexure angles in straight geometries enhance the energy dissipation capabilities of the structure under both quasi static and dynamic loading conditions.

4.4.8 Resulting relation between angle for curved flexures

The curved samples also exhibit an increasing trend in energy dissipation as the flexure angle increases. However, for the dynamically tested samples, this trend does not continue linearly to the highest tested angle. Instead, energy dissipation reaches an optimum before the steepest flexure angle of 60 degrees is reached. At higher angles, the energy dissipation either plateaus or slightly decreases, depending on the impact energy.

This behaviour can be attributed to the deformation mechanics of the curved geometry. At the low impact energy of 0.4 J, samples, especially those with higher flexure angles, did not deform significantly. Instead, the hammer often bounced back after minimal compression of the sample, resulting in very low energy dissipation. This is due to the fact that the impact energy was insufficient to overcome the initial stiffness threshold of the flexure.

As the impact energy increased, the samples began to deform more significantly. In 0.8 J impact energy tests, partial deformation was observed. Typically, only one of the three layers deformed under impact. This layered deformation is consistent with what was observed in the quasi static tests, where higher angle curved samples showed sequential activation of the layers. Because not the full sample was being deformed, energy absorption was better, but still limited at this impact energy.

At optimal impact energies, different for every angle, full deformation was achieved, leading to maximum energy dissipation. The impact energy of the hammer would fully deform the sample, and return almost no energy back to the hammer. This can most clearly be seen for the samples at 36.25 and 45 degrees for an impact energy of 1.2 J. Where energy dissipation of nearly a 100 % was achieved. This high performance is related to the retained deformation behaviour described earlier.

Beyond this point, further increases in impact energy led to reduced energy absorption. This is due to the excess impact energy is not able to be absorbed by the sample but instead causing the hammer to bounce back, of the frame instead of the sample. This behaviour is particularly prominent in high angle samples.

Overall, the curved flexures demonstrate a more complex relationship between flexure angle and energy dissipation than their straight counterparts. While increasing the angle generally enhances energy absorption, the presence of negative stiffness results in a non-linear response pattern that peaks at 36.25 and 45 degrees.

The linear relationship between flexure angle and energy absorption is inconsistent with findings from the literature review (see chapter 2). The results from Series A2 do not align with this hypothesized behaviour, only partial alignment holds for the samples tested under dynamic testing. The relation did hold for the quasi static testing.

4.4.9 Resulting difference between curved and straight flexures

A key distinction between the curved and straight flexure samples can be observed in their behaviour during the unloading phase of quasi static testing. Specifically, only the high angle curved samples and the 60 degree straight sample exhibit a region of negative stiffness in their force-displacement response. Notably, the negative stiffness characteristics disappear for lower angles but where more prominently present in the curved samples compared to the straight ones.

This results in a difference in post impact behaviour during dynamic testing, as clearly illustrated in Figure 4.17, where the energy dissipation performance of both curved and straight samples is compared for the range of angles. The curved samples exhibit consistently higher energy dissipation, particularly in regions where the impact energy is well-matched to the structural response, where retained deformation occurs. This trend is not observed in the quasi static tests. As shown in Figure 4.10, both straight and curved samples display similar linear behaviour. Although the curved samples demonstrate higher energy dissipation overall, the distinct behavioural differences seen in the dynamic tests are not present under quasi static testing.

Overall, this unique combination of increased negative stiffness and controlled retained deformation in curved samples leads to superior energy absorption performance. Straight samples, which lack these characteristics, exhibit a more linear but limited energy dissipation profile. Nonetheless, both sample series demonstrate that, in general, increasing the flexure angle results in greater energy dissipation.

4.4.10 Resulting relation between thickness for straight flexures

For Series B, where the flexure angle was held constant, and only the flexure thickness was varied, the results suggest that thickness has a limited effect on energy dissipation performance. In the quasi static tests, as shown in Figure 4.11, the energy dissipation remained largely consistent across all tested thicknesses. This implies that under slow loading conditions, variations in thickness do not significantly influence the energy absorption capacity.

A similar trend is observed in the dynamic test results, presented in Figure 4.18. Here, energy dissipation shows a slight downward trend with increasing thickness, though the variation is small and not significant. This further supports the conclusion that, within the tested range, thickness is not a dominant parameter affecting energy dissipation.

Notably, the level of impact energy did have a greater influence on energy dissipation than thickness itself. The data reveal that at an intermediate impact energy of 0.8 J, samples dissipated the least energy, whereas both lower 0.4 J and higher 1.2 and 1.6 J impact energies resulted in greater energy dissipation. This trend suggests that, similar to the curved samples, optimal energy dissipation occurs when the impact energy is matched to the sample's structural response.

In summary, while increasing thickness raises the stiffness of the flexures, which in turns requires a greater force for compression. It does not significantly alter their energy absorption performance. Therefore, within the parameters tested, thickness can be considered largely independent of the energy dissipation behaviour.

4.5 Conclusion

This section investigated the energy dissipation behaviour of 3D-printed TPU flexures under both quasi static and dynamic testing, with a focus on the influence of parameters such as flexure angle, geometry, and thickness. The results demonstrate that flexure angle is the most significant design variable affecting energy dissipation, followed closely by the introduction of curvature in the flexures. In contrast, thickness appears to have a negligible impact on energy dissipation within the tested range and can be considered largely independent of the energy dissipation behaviour.

Varying the angle of straight flexures resulted in a near-linear increase in energy dissipation with respect to flexure angle, consistent across both quasi static and dynamic testing. Curved flexures, however, exhibited more complex behaviour. Although increasing the angle generally enhanced energy absorption, the presence of negative stiffness and retained deformation led to non-linear trends with distinct optimal points. Notably, curved samples demonstrated the highest overall energy dissipation, particularly at a flexure angle of 45 degrees with 1.2 J of impact energy.

The flexure thickness of the samples did not significantly influence the energy dissipation capabilities. Although thicker samples exhibited greater stiffness and required more force to compress, their total energy dissipation remained largely unchanged in both the quasi static and dynamic tests.

Dynamic testing revealed that energy dissipation is strongly influenced by the impact energy. Optimal dissipation occurred when the impact energy matched the structural response of the flexure, allowing it to compress fully without significant remaining energy. Furthermore, the results showed that quasi static testing, although commonly used, does not always accurately represent material behaviour under high velocity impact conditions. This highlights the importance of dynamic testing for evaluating energy absorption applications.

In conclusion, the studied energy absorption capabilities of mechanical metamaterials are governed primarily by flexure angle, and to a lesser extent by curvature. Negative stiffness and retained deformation behaviour observed in curved geometries present valuable design features for achieving near total energy dissipation during impact. These findings offer useful guidelines for the design of tuneable, impact-absorbing metamaterials.

Chapter 5

Final remarks

5.1 Discussion

This thesis investigated energy absorbing mechanical metamaterials, specifically bistable triangle flexures, to address and identify the parameters that influence the energy dissipation. To achieve this, a new, non-destructive dynamic impact tester, inspired by the Charpy impact test, was developed. This device offers an improved balance between simplicity, precision, and data acquisition compared to existing dynamic impact testing methods.

Experimental testing of 3D-printed TPU flexures revealed the flexure angle as the most significant design variable, where a steeper angle of the flexure resulted in a higher energy dissipation. In contrast, flexure thickness had a negligible impact. A critical finding was the substantially higher energy dissipation observed in dynamic tests of 70 % to a 100 %, compared to tradition quasi static tests which had a dissipation of 40 % to 60 %, underscoring the necessity of dynamic testing for real world impact applications.

5.2 Conclusion

In conclusion, this thesis advanced the understanding of energy absorbing mechanical metamaterials. It established the influence of flexure angle and flexure design on energy dissipation. Identified negative stiffness and retained deformation as key causes for achieving near total energy absorption. And highlighted the importance of doing dynamic test for impact absorbing development. These findings provide design guidelines for developing, reusable, and efficient impact absorbing structures.

Acknowledgements

After ten years, I am proud to conclude my studies at TU Delft. It has been a long journey marked by challenges, lessons, and growth. But I am proud to say that I have made it to the finish line. Completing this thesis signifies the closing of an important chapter in my life. I would like to express my gratitude to those who supported me throughout this process and helped made this achievement possible.

First and foremost, I would like to sincerely thank my supervisor, Freek. Thank you for your guidance, and steady encouragement throughout this final year. Your insights and support helped shape my ideas and move this thesis forward, even when things did not go as planned.

A big thank you to Patrick for spending countless hours with me at the tensile tester, measuring a lot of samples, and making sure we got the data we needed. Your help made the testing process not only more efficient, but also a lot more enjoyable.

I would also like to thank Dante for providing the best 3D printing service I could have asked for. While other suppliers could not deliver, you consistently came through. Without your help, I would probably still be stuck waiting in line elsewhere.

To all my friends, thank you for putting the fun in studying. Your support and the good times we shared turned this period into something I truly do not want to forget.

To my parents and family, thanks so much for sticking with me and being patient, even though this academic journey took longer than I expected. Your support and belief in me never faded, and that really kept me going.

To everyone who contributed in any way, large or small, thank you. I truly could not have done it without you.

And finally, to Puck, my girlfriend and support during the final stretch. Thank you for your love, encouragement, and for standing by me through it all. Your support in these last few months helped me get to the finish line.

.

Bibliography

Biffi, C., Soyarslan, C., Fiocchi, J., Bregoli, C., du Plessis, A., Tuissi, A., and Mehrpouya, M. (2024). Additive manufacturing of NiTi architected metamaterials. *Additive Manufacturing Letters*, 10. Publisher: Elsevier B.V.

Broeren, F. G., Van Der Wijk, V., and Herder, J. L. (2020-02). Spatial pseudo-rigid body model for the analysis of a tubular mechanical metamaterial. *Mathematics and Mechanics of Solids*, 25(2):305–316.

Che, K., Yuan, C., Qi, H., and Meaud, J. (2018). Viscoelastic multistable architected materials with temperature-dependent snapping sequence. *Soft Matter*, 14(13):2492–2499. Publisher: Royal Society of Chemistry.

Che, K., Yuan, C., Wu, J., Qi, H., and Meaud, J. (2017). Three-dimensional-printed multistable mechanical metamaterials with a deterministic deformation sequence. *Journal of Applied Mechanics, Transactions ASME*, 84(1). Publisher: American Society of Mechanical Engineers (ASME).

Chen, Q., Zhang, X., and Zhu, B. (2018). Design of buckling-induced mechanical metamaterials for energy absorption using topology optimization. *Structural and Multidisciplinary Optimization*, 58(4):1395–1410. Publisher: Springer Verlag.

Chen, S., Lian, X., Zhu, S., Li, M., Wang, B., and Wu, L. (2023). A re-usable negative stiffness mechanical metamaterial composed of bi-material systems for high energy dissipation and shock isolation. *Composite Structures*, 322. Publisher: Elsevier Ltd.

Chen, T., Zhang, X., Yan, X., Zhang, B., Jiang, J., Huang, D., Qi, M., and Sun, R. (2019). Harnessing magnets to design tunable architected bistable material. *Advanced Engineering Materials*, 21(3). Publisher: Wiley-VCH Verlag.

Feng, L., Yu, G., Ma, L., Wu, L., and Zhang, A. (2020). Enhanced design of hourglass truss sandwich structures for compressive resistance. *Science China Technological Sciences*, 63(12):2717–2728. Publisher: Springer Verlag.

Findeisen, C., Hohe, J., Kadic, M., and Gumbsch, P. (2017). Characteristics of mechanical metamaterials based on buckling elements. *Journal of the Mechanics and Physics of Solids*, 102:151–164. Publisher: Elsevier Ltd.

Garanger, K., Del Valle, I., Rath, M., Krajewski, M., Raheja, U., Pavone, M., and Rimoli, J. (2021). Soft tensegrity systems for planetary landing and exploration. In van Susante P.J. and Roberts A.D., editors, *Earth Space: Space Explor., Utili., Eng., Constr. Extrem. Environ. - Sel. Pap. Bienn. Int. Conf. Eng., Sci., Constr., Oper. Challenging Environ.*, pages 841–854. American Society of Civil Engineers (ASCE). Journal Abbreviation: Earth Space: Space

Explor., Utili., Eng., Constr. Extrem. Environ. - Sel. Pap. Bienn. Int. Conf. Eng., Sci., Constr., Oper. Challenging Environ.

Gavazzoni, M., Foletti, S., and Pasini, D. (2022). Cyclic response of 3d printed metamaterials with soft cellular architecture: The interplay between as-built defects, material and geometric non-linearity. *Journal of the Mechanics and Physics of Solids*, 158. Publisher: Elsevier Ltd.

Giri, T. and Mailen, R. (2021). Controlled snapping sequence and energy absorption in multistable mechanical metamaterial cylinders. *International Journal of Mechanical Sciences*, 204. Publisher: Elsevier Ltd.

Haghpanah, B., Salari-Sharif, L., Pourrajab, P., Hopkins, J., and Valdevit, L. (2016). Architected materials: Multistable shape-reconfigurable architected materials (adv. mater. 36/2016). *Advanced Materials*, 28(36):8065. Publisher: Wiley-VCH Verlag.

Haron, A. and Ismail, K. A. (2012-09-18). Coefficient of restitution of sports balls: A normal drop test. *IOP Conference Series: Materials Science and Engineering*, 36:012038.

Hou, X. and Silberschmidt, V. V. (2015). Metamaterials with negative poisson's ratio: A review of mechanical properties and deformation mechanisms. *Mechanics of Advanced Materials: Analysis of Properties and Performance*, pages 155–179.

Hou, Z., Duan, C., Yu, Y., and Wang, Z. (2023). Reusable and efficient energy-absorbing architected materials via synergy of snap-through instability and inter-locking mechanism. *Extreme Mechanics Letters*, 58. Publisher: Elsevier Ltd.

Jafarabadi, A., Ferretto, I., Mohri, M., Leinenbach, C., and Ghafoori, E. (2023). 4d printing of recoverable buckling-induced architected iron-based shape memory alloys. *Materials and Design*, 233. Publisher: Elsevier Ltd.

Ju, X., Li, S., Zhang, Y., Wu, P., and Li, Y. (2024). Design of multi-stable metamaterial cell with improved and programmable energy trapping ability based on frame reinforced curved beams. *Thin-Walled Structures*, 202. Publisher: Elsevier Ltd.

Kappe, K., Wahl, J., Gutmann, F., Boyadzhieva, S., Hoschke, K., and Fischer, S. (2022). Design and manufacturing of a metal-based mechanical metamaterial with tunable damping properties. *Materials*, 15(16). Publisher: MDPI.

Karagiozova, D., Zhang, J., Lu, G., and You, Z. (2019). Dynamic in-plane compression of miura-ori patterned metamaterials. *International Journal of Impact Engineering*, 129:80–100. Publisher: Elsevier Ltd.

Li, Q., Tian, W., Wu, D., and Gao, W. (2023). Nonlinear dynamic stability analysis of imperfect architected cellular sandwich plate under impact loading. *Acta Mechanica Sinica/Lixue Xuebao*, 39(4). Publisher: Springer Verlag.

Li, S., Fang, H., Sadeghi, S., Bhovad, P., and Wang, K.-W. (2019). Architected origami materials: How folding creates sophisticated mechanical properties. *Advanced Materials*, 31(5). Publisher: Wiley-VCH Verlag.

Liang, K., Zhou, S., Luo, Y., Zhang, X., and Kang, Z. (2024). Topology optimization design of recoverable bistable structures for energy absorption with embedded shape memory alloys. *Thin-Walled Structures*, 198. Publisher: Elsevier Ltd.

Meng, Z., Liu, M., Zhang, Y., and Chen, C. (2020). Multi-step deformation mechanical metamaterials. *Journal of the Mechanics and Physics of Solids*, 144. Publisher: Elsevier Ltd.

Mohan, A., Srinivasan, S., and Joshi, M. (2017). Exploitation of large recoverable deformations using weaved shape memory alloy wire-based sandwich panel configurations. *Journal of Engineering Materials and Technology, Transactions of the ASME*, 139(2). Publisher: American Society of Mechanical Engineers (ASME).

Montanari, M., Brighenti, R., and Spagnoli, A. (2023). Defect sensitivity mitigation in the compressive mechanical response of two-phase lattice metamaterials. *Composite Structures*, 323. Publisher: Elsevier Ltd.

Nian, Y., Wan, S., Avcar, M., Yue, R., and Li, M. (2023). 3d printing functionally graded metamaterial structure: Design, fabrication, reinforcement, optimization. *International Journal of Mechanical Sciences*, 258. Publisher: Elsevier Ltd.

Osman, M., Shazly, M., El-Danaf, E., Jamshidi, P., and Attallah, M. (2020). Compressive behavior of stretched and composite microlattice metamaterial for energy absorption applications. *Composites Part B: Engineering*, 184. Publisher: Elsevier Ltd.

Pajunen, K., Johanns, P., Pal, R., Rimoli, J., and Daraio, C. (2019). Design and impact response of 3d-printable tensegrity-inspired structures. *Materials and Design*, 182. Publisher: Elsevier Ltd.

Qiang, W., Durandet, Y., Zhang, X., and Lu, G. (2024). Experimental and numerical study on energy absorption performance of truncated origami materials. *Thin-Walled Structures*, 200. Publisher: Elsevier Ltd.

Queheillalt, D. and Wadley, H. (2011). Hollow pyramidal lattice truss structures. *International Journal of Materials Research*, 102(4):389–400.

Rimoli, J. (2018). A reduced-order model for the dynamic and post-buckling behavior of tensegrity structures. *Mechanics of Materials*, 116:146–157. Publisher: Elsevier B.V.

Saba, N., Jawaid, M., and Sultan, M. (2019). An overview of mechanical and physical testing of composite materials. In *Mechanical and Physical Testing of Biocomposites, Fibre-Reinforced Composites and Hybrid Composites*, pages 1–12. Elsevier.

Shen, J., Zhou, S., Huang, X., Ruan, D., and Xie, Y. (2015). Inertia effect on buckling-induced auxetic metamaterials. *International Journal of Protective Structures*, 6(2):311–322. Publisher: SAGE Publications Inc.

Smith, R. J. (1981). Auto crash tests unsettle japan and detroit. *Science*, 211:150–152.

Tan, X., Chen, S., Wang, B., Zhu, S., Wu, L., and Sun, Y. (2019). Design, fabrication, and characterization of multistable mechanical metamaterials for trapping energy. *Extreme Mechanics Letters*, 28:8–21. Publisher: Elsevier Ltd.

Tan, X., Li, Y., Wang, L., Yao, K., Ji, Q., Wang, B., Laude, V., and Kadic, M. (2023). Bioinspired flexible and programmable negative stiffness mechanical metamaterials. *Advanced Intelligent Systems*, 5(6). Publisher: John Wiley and Sons Inc.

Tan, X., Wang, L., Zhu, S., Chen, S., Wang, B., and Kadic, M. (2022). A general strategy for performance enhancement of negative stiffness mechanical metamaterials. *European Journal of Mechanics, A/Solids*, 96. Publisher: Elsevier Ltd.

Tian, W., Li, Q., Wang, Q., Chen, D., and Gao, W. (2024). Additive manufacturing error quantification on stability of composite sandwich plates with lattice-cores through machine learning technique. *Composite Structures*, 327. Publisher: Elsevier Ltd.

Uddin, M., Barsoum, I., Kumar, S., and Schiffer, A. (2024). Enhancing compressive performance in 3d printed pyramidal lattice structures with geometrically tailored i-shaped struts. *Materials and Design*, 237. Publisher: Elsevier Ltd.

Wang, Y., Ramirez, B., Carpenter, K., Naify, C., Hofmann, D., and Daraio, C. (2019). Architected lattices with adaptive energy absorption. *Extreme Mechanics Letters*, 33. Publisher: Elsevier Ltd.

Xiao, Z., Wang, L., Zhang, Y., and Yang, C. (2022-01-02). A study on motorcyclist head reponses during impact against front end of vehicle. *International Journal of Crashworthiness*, 27(1):147–159. Publisher: Informa UK Limited.

Xu, R., He, Y., Li, X., Lu, M., and Chen, Y. (2023). Snap-fit mechanical metamaterials. *Applied Materials Today*, 30. Publisher: Elsevier Ltd.

Yang, B., Dai, K., Li, C., Yu, D., Zhang, A., Cheng, J., and Zhang, H. (2024). Lightweight recoverable mechanical metamaterials for efficient buffering of continuous multi extreme impacts. *Sustainable Materials and Technologies*, 39. Publisher: Elsevier B.V.

Yao, H., Zhao, X., Shi, K., Sun, W., and Mi, S. (2024a). Programmable and resilient metamaterials with anisotropic and non-linear mechanical responses composed exclusively of stiff constituents. *Materials Horizons*, 11(19):4689–4704.

Yao, X., Dong, Q., Li, X., and Hu, N. (2024b). Design and characterization of architected cellular composite material embedded with strain rate dependent foam. In Papadikis K., Zhang C., Tang S., Liu E., and Di Sarno L., editors, *Lect. Notes Civ. Eng.*, volume 393, pages 641–650. Springer Science and Business Media Deutschland GmbH. Journal Abbreviation: Lect. Notes Civ. Eng.

Yao, X., Liu, K., Dong, Q., Li, X., Ma, C., and Hu, N. (2024c). Tunable and recoverable energy absorption of foam-embedded architected cellular composite material at multiple strain rates. *Composite Structures*, 329. Publisher: Elsevier Ltd.

Yazdani Sarvestani, H., Akbarzadeh, A., Niknam, H., and Hermenean, K. (2018). 3d printed architected polymeric sandwich panels: Energy absorption and structural performance. *Composite Structures*, 200:886–909. Publisher: Elsevier Ltd.

Zhang, J., Ohsaki, M., Rimoli, J., and Kogiso, K. (2021). Optimization for energy absorption of 3-dimensional tensegrity lattice with truncated octahedral units. *Composite Structures*, 267. Publisher: Elsevier Ltd.

Zhang, W., Yan, Z., Zhang, J., Wang, H., Han, F., Jiang, P., Wu, T., and Qin, Q. (2024). On in-plane crushing behavior of an improved double-arrow auxetic metamaterial with two-step deformation mode. *Engineering Structures*, 303. Publisher: Elsevier Ltd.

Zhang, X., Wang, M., Tang, W., and Wang, J. (2019). A flexible measurement technique for testing mass and center of gravity of large-sized objects. *Measurement Science and Technology*, 31.

Zhang, X., Yao, J., Liu, B., Yan, J., Lu, L., Li, Y., Gao, H., and Li, X. (2018). Three-dimensional high-entropy alloy-polymer composite nanolattices that overcome the strength-recoverability trade-off. *Nano Letters*, 18(7):4247–4256. Publisher: American Chemical Society.

Appendix A: Literature analysis data

Publication Year	Author	ISSN / ISBN	2D	2.5D	3D	-10% dissipated	5% dissipated	10% dissipated	25% dissipated	33% dissipated	50% dissipated	75% dissipated	90% dissipated	200% dissipated	NaN% dissipated	Not Bistable	Bistable	Biway Bistable	Triway bistable	Multi stable	Complexity 2	Complexity 3	Complexity 4	Complexity 6	Complexity 8	Complexity 9	Complexity 10	Complexity 11	Complexity 12	Complexity 14	Complexity 18	Complexity 20	Complexity 21	Complexity 22	Complexity 24	Complexity 27	Complexity 28	Complexity 30	Complexity 32	Complexity 36	Complexity 38	Complexity 40	Complexity 50	Complexity 54	Complexity 60	Complexity NaN	Negative DOF	Zero DOF	One DOF	Two DOF	Three DOF	Multiple DOF	NaN DOF	Not readable	Not availible	Not relevant
2022	Guo, S.; Gao,	02638231 (ISSN)			y				y										y																																				
2024	Yang, H.; Liu, Z	13598368 (ISSN)	y												y																									y										y					
2021	Garanger, K.; I	978-078448337-4 (ISBN)													y																							y									y							
2021	Zhang, J.; Ohs	02638223 (ISSN)			y										y																							y									y							
2016	Rimoli, J.J.	978-162410392-6 (ISBN)			y										y																							y									y							
2019	Pajunen, K.; Jo	02641275 (ISSN)			y			y							y																							y									y							
2018	Rimoli, J.J.	01676636 (ISSN)			y										y																							y									y							
2024	Feng, X.; Sher	23520124 (ISSN)			y										y																							y									y							
2018	Zhang, X.; Yao	15306984 (ISSN)			y						y				y																								y								y							
2021	Khajehtourian,	22969144 (ISSN)	y													y																					y													y				
2024	Zheng, H.; Sur	0734743X (ISSN)			y											y																				y													y				
2016	Haghpanah, B	09359648 (ISSN)	y										y			y		y																	y						y					y	y						
2020	Vangelatos, Z.	14381656 (ISSN)			y										y																			y																	y			
2021	Bauer, J.; Krau	09359648 (ISSN)			y										y																		y				y									y							
2024	Yao, H.; Zhao,	20516347 (ISSN)			y										y																		y																		y			
2022	Hao, J.; Han, D	01410296 (ISSN)	y												y																		y																		y			
2020	Osman, M.M.;	13598368 (ISSN)			y										y																		y														y							
2019	Wang, Y.; Ran	23524316 (ISSN)			y							y			y																		y														y							
2023	Xu, R.; He, Y.;	23529407 (ISSN)			y	y													y																										y						y			
2023	Yang, K.; Li, X.	20711050 (ISSN)			y										y																														y	y							
2019	Tan, X.; Wang,	00207403 (ISSN)	y													y																														y		y						
2011	Li, M.-Z.; Stepl	15272648 (ISSN)			y										y																														y						y		
2016	Haghpanah, B	09359648 (ISSN)	y		y											y																														y		y						
2024	Qiang, W.; Dur	02638231 (ISSN)													y																														y						y		
2022	Jia, Z.; Liu, F.;	02638223 (ISSN)			y										y																														y						y		
2019	Karagiozova, D	0734743X (ISSN)			y										y																														y						y		
2019	Tan, X.; Chen,	23524316 (ISSN)			y										y																														y	y							
2024	Yang, H.; Zhar	1616301X (ISSN)			y							y				y																														y	y							
2019	Rhodes, T.; Go	22969144 (ISSN)			y										y																														y	y							
2022	Chen, X.; Ji, Q	00225096 (ISSN)			y										y																														y	y							
2019	Li, S.; Fang, H	09359648 (ISSN)			y											y																														y						y		
2022	Ma, J.; Jiang, J	23524316 (ISSN)			y											y																														y		y						
2021	Gao, R.; Guo,	02638231 (ISSN)			y											y																		y															y						
2020	Jin, L.; Khajeh	00278424 (ISSN)	y													y		y														y																				y				
2021	Shi, J.; Mofatte	09359648 (ISSN)			y					y						y	y	y													y										y		y		y		y						
2021	Damodaran, V	02641275 (ISSN)			y											y															y																	y						
2022	Pechac, J.E.; F	23524316 (ISSN)			y			y							y															y																					y				
2024	Yang, B.; Dai,	22149937 (ISSN)			y											y															y																				y				
2020	Ni, B.; Gao, H.	00218936 (ISSN)			y											y															y																				y				
2023	Dong, Y.; Yu, T	02638223 (ISSN)			y											y															y																				y				
2017	Findeisen, C.;	00225096 (ISSN)			y					y						y															y																				y				
2023	Tan, X.; Li, Y.;	26404567 (ISSN)			y				y							y															y																				y				
2024	Li, Z.; Li, X.; G	02638231 (ISSN)			y											y													y																				y					
2024	Hou, X.; Shen	02638223 (ISSN)	y													y												y																							y				
2020	Yang, W.; Xion	10996362 (ISSN)			y										y												y																						y					
2023	Chawla, K.; Gu	19360851 (ISSN)			y										y													y																						y				
2023	Li, Q.; Tian, W.	05677718 (ISSN)			y										y												y					y																y					
2022	Kappe, K.; Wa	19961944 (ISSN)		y					y							y												y																							y				
2024	Tian, W.; Li, Q.	02638223 (ISSN)			y										y													y						y															y				
2023	Chen, S.; Lian	02638223 (ISSN)	y						y										y									y																							y				
2019	Feng, L.-J.; We	00207403 (ISSN)			y										y											y						y																	y				
2024	Yao, X.; Liu, K.	02638223 (ISSN)	y							y						y										y																								y				
2022	Xiu, H.; Liu, H.	00278424 (ISSN)	y													y										y																										y			
2024	Chai, Z.; Zong	09359648 (ISSN)	y													y										y																											y			
2022	Jeon, S.-Y.; Sh	09359648 (ISSN)	y													y										y																										y			
2021	Mehreganian,	00218936 (ISSN)	y													y										y																										y			
2024	Liu, T.; Deng, F	00207403 (ISSN)	y													y										y																										y			
2015	Shan, S.; Kang	09359648 (ISSN)	y													y										y																										y			
2020	Meng, Z.; Liu,	00225096 (ISSN)	y													y										y																											y			
2023	Yu, J.; Shi, X.;	23524316 (ISSN)	y													y										y																										y			
2023	Mehreganian,	00207683 (ISSN)	y													y										y																										y			
2018	Debeau, D.A.;	08842914 (ISSN)	y													y										y																										y			
2011	Queheillalt, D.	18625282 (ISSN)			y										y											y																										y			
2019	Chen, T.; Zhan	14381656 (ISSN)	y													y										y																											y			
2024	Aewzipo, N.; C	09641726 (ISSN)	y													y										y																										y			
2017	Mohan, A.; Sri	00944289 (ISSN)			y					y					y											y																										y			
2023	Zhao, A.; Liu, (	02638223 (ISSN)	y													y										y																										y			
2024	Uddin, M.A.; B	02641275 (ISSN)			y										y											y																										y			
2020	Feng, L.J.; Yu,	16747321 (ISSN)			y										y											y						y			y		y												y			
2023	Gan, J.; Li, F.;	02663538 (ISSN)	y													y										y																										y			
2024	Ju, X.; Li, S.; Z	02638231 (ISSN)	y					y								y										y																										y			
2019	Darwish, Y.; El	15732487 (ISSN)	y											y		y										y																										y			
2023	Jafarabadi, A.;	02641275 (ISSN)	y						y							y										y																											y			
2012	Liu, J.; Pattofa	2100014X (ISSN)			y										y										y																										y			
2007	Tang, X.; Prak	13596454 (ISSN)			y										y										y																										y			
2019	Francesconi, L	23524316 (ISSN)			y										y									y																											y			

Publication Year	Author	ISSN / ISBN	2D	2.5D	3D	-10% dissipated	5% dissipated	10% dissipated	25% dissipated	33% dissipated	50% dissipated	75% dissipated	90% dissipated	200% dissipated	NaN% dissipated	Not Bistable	Bistable	Biway Bistable	Triway bistable	Multi stable	Complexity 2	Complexity 3	Complexity 4	Complexity 6	Complexity 8	Complexity 9	Complexity 10	Complexity 11	Complexity 12	Complexity 14	Complexity 18	Complexity 20	Complexity 21	Complexity 22	Complexity 24	Complexity 27	Complexity 28	Complexity 30	Complexity 32	Complexity 36	Complexity 38	Complexity 40	Complexity 50	Complexity 54	Complexity 60	Complexity NaN	Negative DOF	Zero DOF	One DOF	Two DOF	Three DOF	Multiple DOF	NaN DOF	Not readable	Not availible	Not relevant
2024	Liang, K.; Zhou	02638231 (ISSN)	y			y										y								y																														
2017	Che, K.; Yuan,	00218936 (ISSN)	y													y								y																										y					
2022	Yin, Y.; Yu, Y.;	19475411 (ISSN)		y												y								y																														
2024	Ma, X.; Zhang,	02638231 (ISSN)			y											y								y														y							y									
2022	Deng, B.; Zare	09359648 (ISSN)	y													y								y																														
2015	Shen, J.; Zhou	20414196 (ISSN)	y		y											y								y						y																							
2024	Yao, X.; Dong,	23662557 (ISSN); 978-981	y														y							y																								y					
2021	Giri, T.R.; Mail	00207403 (ISSN)	y					y		y							y							y																											y			
2022	Tung, C.-C.; C	02641275 (ISSN)			y			y								y								y																													
2022	Tan, X.; Wang,	09977538 (ISSN)	y								y						y							y																												y		
2021	Glaesener, R.M	00225096 (ISSN)	y													y							y																												y		
2018	Che, K.; Yuan,	1744683X (ISSN)	y														y							y																													
2019	Kumar, S.; Uba	19448244 (ISSN)	y													y								y																												y		
2023	Xu, Y.; Huang,	25902393 (ISSN)	y													y								y																												y		
2022	J, J.A.; Schnei	00207403 (ISSN)		y												y								y																												y		
2024	Jin, M.; Hou, X	09641726 (ISSN)	y			y											y							y																											y			
2023	Hou, Z.; Duan,	23524316 (ISSN)	y				y										y							y																											y			
2024	Zhang, W.; Yar	01410296 (ISSN)	y													y								y																											y			
2020	Casalotti, A.; D	02638223 (ISSN)	y													y								y																												y		
2024	Du, Z.; Bian, T	20950349 (ISSN)	y													y								y																											y			
2023	Chapa, A.; Cua	13552546 (ISSN)	y					y								y								y																												y		
2018	Chen, Q.; Zhai	1615147X (ISSN)	y														y							y																											y			
2022	Gavazzoni, M.	00225096 (ISSN)	y												y	y					y			y																											y		y		
2020	Vangelatos, Z.	0277786X (ISSN)	y													y								y																												y		
2024	Li, Q.; Li, P.; G	24680133 (ISSN)	y													y								y																													y		
2022	Dong, J.; Hu, (	02638223 (ISSN)	y													y						y																														y		
2021	Wang, Y.; Chi,	02638223 (ISSN)	y													y						y																														y		
2018	Niknam, H.; Ak	02638223 (ISSN)	y													y						y																															y		
2020	Wadee, M.A.; I	22968016 (ISSN)	y													y						y																															y		
2024	Biffi, C.A.; Soy	27723690 (ISSN)		y				y								y						y																															y		
2023	Montanari, M.;	02638223 (ISSN)	y													y					y																													y				
2022	Carstensen, J.	13596462 (ISSN)	y													y				y			y	y																											y	y			
2021	Liu, Y.; Lei, M.;	09641726 (ISSN)	y													y				y																															y			
2021	Chen, Y.; Jin, L	1616301X (ISSN)		y			y									y				y																															y			
2018	Vuyk, P.; Cui, S	14381656 (ISSN)	y													y				y																															y			
2024	Yan, S.; Liu, W	13697021 (ISSN)	y					y								y				y																															y			
2017	Li, T.; Wang, L.	02638223 (ISSN)	y													y				y			y																												y		y		
2019	Goyal, R.; Per	09560599 (ISSN)																																																				y
2019	Morris, C.; Bek	14381656 (ISSN)																																																			y
2020	Kim, W.-B.; Ha	2072666X (ISSN)																																																			y
2020	Zhang, G.; Kha	1615147X (ISSN)																																																			y
2022	Tang, Y.; Li, M.	09359648 (ISSN)																																																			y
2021	Tabatabaei, M.	22110984 (ISSN)																																																			y
2019	Nwe Nwe, M.T	978-078448222-3 (ISBN)																																																			y
2024	Wang, Z.; Sun	02638231 (ISSN)																																																			y
2023	Xu, R.; Chen, (	26318644 (ISSN)																																																			y
2011	Jiang, T.; Xue,	10226680 (ISSN);																																																			y
2013	Herencia, J.E.;	16151488 (ISSN)																																																			y
2010	Enrique Heren	978-160086954-9 (ISBN)																																																			y
2022	Li, C.; Peng, Z	25902393 (ISSN)																																																			y
1993	Salama, M.; Ui	09641726 (ISSN)																																																			y
2020	Dulhani, D.; Se	0094243X (ISSN)																																																			y
2022	Li, L.; Kim, S.;	19424302 (ISSN)																																																				y
2019	Fu, K.; Zhao, Z	1616301X (ISSN)																																																				y
2012	Xu, Y.J.; Doma	17593433 (ISSN);																																																				y
2011	Morka, A.; Dzie	1743355X (ISSN)																																																				y
2022	Aela, P.; Zong,	08991561 (ISSN)																																																				y
2022	Fan, H.; Tian, `	15376494 (ISSN)			y												y																																	y				
2024	Wang, G.; Li, D	09359648 (ISSN)																																																				y
2019	Yang, N.; Zhan	20452322 (ISSN)																																																			y
2017	Blachowski, B.	05536626 (ISSN)																																																			y
2016	Xu, R.; Li, D.; I	09544100 (ISSN)																																																				y
1999	Izumi, K.; Taka	04247760 (ISSN)																																																				y
2019	Vangelatos, Z.	10812865 (ISSN)																																																				y
2013	Zhong, X.-Q.; (	16741056 (ISSN)																																																					y
2022	Zhao, S.; Zhan	01410296 (ISSN)																																																					y
2018	Tripathy, L.; Lu	13588265 (ISSN)																																																					y
2019	Clough, E.C.; I	25902393 (ISSN)																																																					y
2021	Hao, X.; Zhu, I	07339445 (ISSN)																																																					y
2022	Hu, C.; Sun, H	10011455 (ISSN)																																																				y	
2022	Yuan, T.; Ren,	04591879 (ISSN)																																																				y	
2024	Kulikowski, J.;	25902393 (ISSN)																																																					y
2023	Liu, Z.; Fang, I	26404567 (ISSN)																																																					y
2015	Szklarski, J.; W	1024123X (ISSN)																																																					y
2021	Patel, S.A.; Pe	978-162410609-5 (ISBN)																																																					y
2012	Dutra, E.; Viter	15257541 (ISSN)																																																					y

Publication Year	Author	ISSN / ISBN	2D	2.5D	3D	-10% dissipated	5% dissipated	10% dissipated	25% dissipated	33% dissipated	50% dissipated	75% dissipated	90% dissipated	200% dissipated	NaN% dissipated	Not Bistable	Bistable	Biway Bistable	Triway bistable	Multi stable	Complexity 2	Complexity 3	Complexity 4	Complexity 6	Complexity 8	Complexity 9	Complexity 10	Complexity 11	Complexity 12	Complexity 14	Complexity 18	Complexity 20	Complexity 21	Complexity 22	Complexity 24	Complexity 27	Complexity 28	Complexity 30	Complexity 32	Complexity 36	Complexity 38	Complexity 40	Complexity 50	Complexity 54	Complexity 60	Complexity NaN	Negative DOF	Zero DOF	One DOF	Two DOF	Three DOF	Multiple DOF	NaN DOF	Not readable	Not availible	Not relevant
2023	Liu, Z.; Fang, H	21983844 (ISSN)																																																					y
2018	Roșca, V.E.; M	13142704 (ISSN)																																																					y
2015	Carniel, T.A.; M	0307904X (ISSN)																																																					y
2021	Prabhakar, P.;	978-171383759-6 (ISBN)																																																			y	
2023	Liu, H.; Yu, J.;	16726553 (ISSN)																																																			y	
2019	Wang, G.; Zho	978-199918100-0 (ISBN)																																																		y	
2021	Derveni, F.; Gr	NaN																																																		y	
2019	Wadee, M.A.; I	978-113838696-9 (ISBN)																																																		y	
2024	Uddin, M.A.; B	978-079188774-5 (ISBN)																																																		y	
2022	Song, Y.; Yang	05776686 (ISSN)																																																		y	
2023	Hertlein, N.; Sl	978-079188736-3 (ISBN)																																																		y	
1998	Goldsworthy, V	00911062 (ISSN)																																																		y	
2008	Lee, D.W.; Ma	0791843041 (ISBN)																																																		y	
2024		22110984 (ISSN); 978-303																																																		y	
2023	Liu, Y.; Shu, D.	17588251 (ISSN)																																																		y	

Appendix B: AN8 Sensor Specification

Angle Position Sensors

AN8 Sensors

Programmable, non-contact magnetic position sensors capable of continuous rotation

Description

The AN8 Series sensors are non-contact, intrinsically linear contact angle position sensors. The sensors operate through the use of Hall Effect technology with magnetic fields generated by permanent magnets. They provide a linear change in voltage output (ratiometric to the input voltage) corresponding to an angular rotation of the input shaft.

Features

- Angular position sensor with high tolerance for misalignment
- Non-contact angular position sensing and full 360° rotation
- Custom programming available for: angle range, slope, PWM output, custom magnets – contact factory
- No mechanical interface means no parts to wear out or jam
- Available with Delphi connector or 12” (305 mm) wire leads
- RoHS compliant
- IP67
- Maximum air gap of 5.5 mm (0.22”)*

Typical Applications

- Implement (fork lift, agricultural trailer hitch, etc.) position sensing
- Steer, throttle by wire
- Gear selection
- Zero-contact encoder alternative
- Replacement for smart bearings
- Outboard trim sensing

Environmental Specifications

Vibration	6g sinusoidal, 8 g RMS axial; 40Hz – 2 kHz all 3 axes
Operating Temperature	-40 °C to 125 °C (-40 °F to 257 °F) with Delphi connectors, -40 °C to 150 °C (-40 °F to 302 °F) with wire leads
Storage Temperature	-40 °C to 150 °C (-40 °F to 302 °F)
Ingress Protection	IP67

Electrical Specifications

Input Voltage	5.0 VDC ± 10%
Output Voltage	10% to 90% of input (see graph for voltage vs. rotation angle characteristics)
Input Current	14 mA typ., 16 mA max.
Output Current	-8 mA to 8 mA
Output Accuarcy	±3.5%
Output Linearity	±3.5%
Maximum Overvoltage	16 VDC
Absolute Max. Output Current	±30 mA
Output Type	Analog (PWM available)

Mechanical Specifications

Housing Material	Glass Reinforced Plastic
Mechanical Travel	0° to 360° (continuous)
Mating Connector	Delphi Metri-pak 150.2 12162185; Terminal 1214075 / 2047680
Maximum Air Gap* *with AS500106 magnet carrier	5.5 mm (0.22")
Maximum Center-To-Center Offset	2 mm radial (magnet to center)

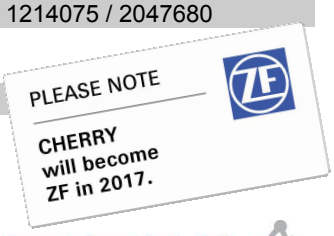

Products

Part Number (Sensor)	Sensor (incl. AS500106 magnet)	Sensing Range	Wires	Connectors	Terminals
AN820001	CU103601	180°	N/A	Packard Metri-pack	1214075 / 2047680
AN820002	CU103602	360°	N/A	Packard Metri-pack	1214075 / 2047680
AN820003*	CU103603	45°	N/A	Packard Metri-pack	1214075 / 2047680
AN820031	--------	180°	18 AWG x 305 mm (12")	N/A	N/A
AN820032	--------	360°	18 AWG x 305 mm (12")	N/A	N/A
AN820033*	--------	45°	18 AWG x 305 mm (12")	N/A	N/A

*Not commonly stocked

Sensor Output

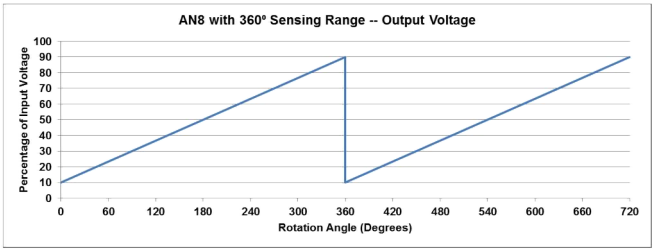

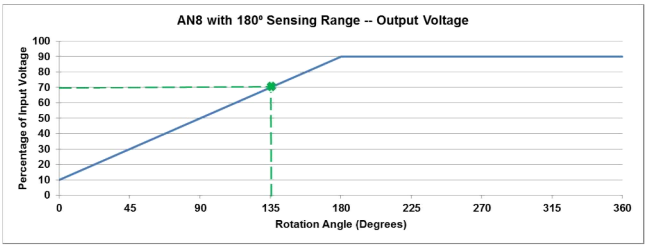

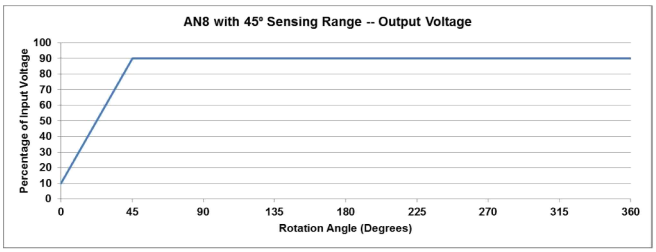

These charts show the output voltage as a percentage of the input voltage for a given angle of rotation.
Example: 180^0 sensing range, magnet rotated 135^0, output voltage will be 70% of input voltage (see dashed lines in graph above).

Dimensions mm (inches)

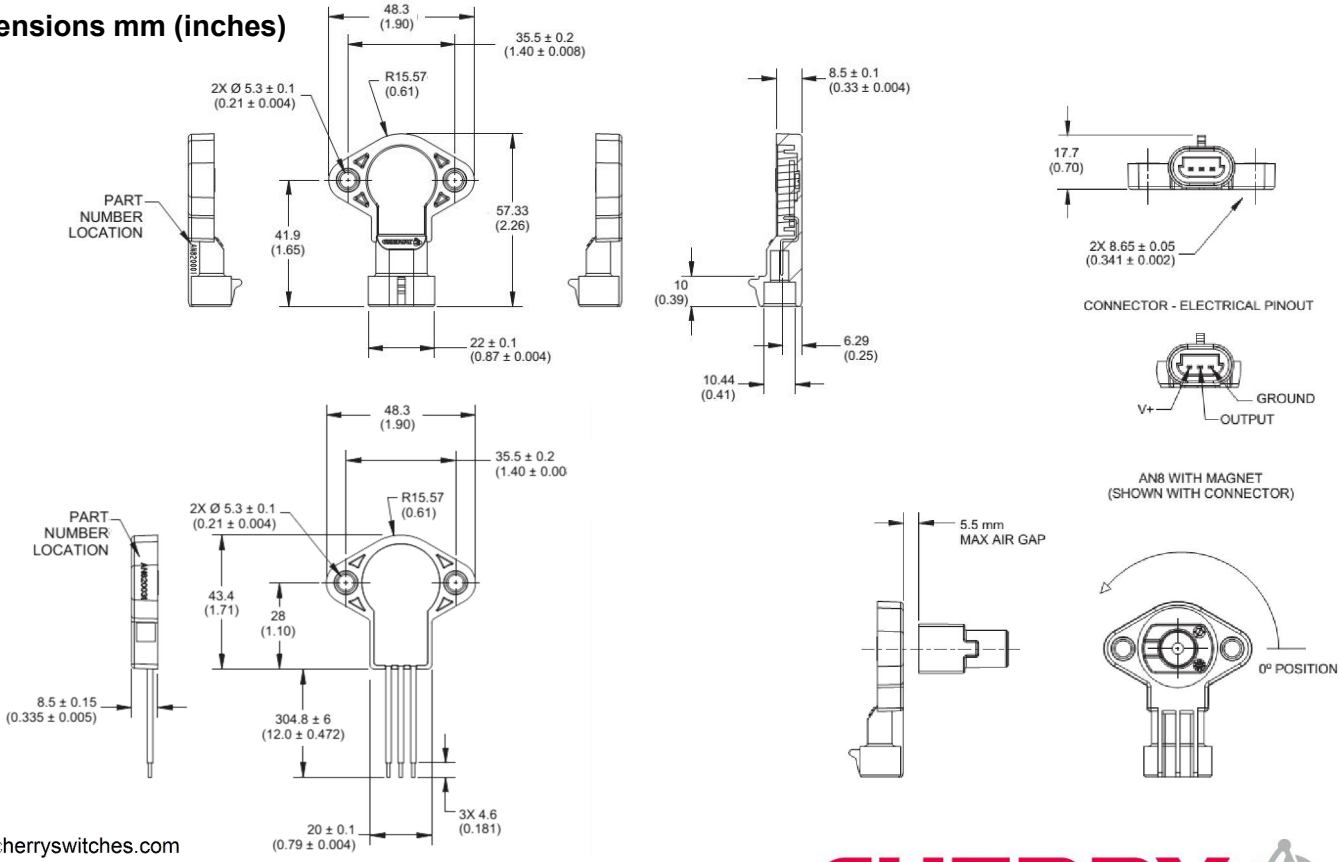

Appendix C: Bambulab TPU A95HF datasheet

Bambu Filament

Technical Data Sheet V1.0

TPU 95A HF

• Basic Info

Bambu TPU 95A HF is an optimized TPU filament designed for high-speed 3D printing. Compared to regular TPU 95A, TPU 95A HF offers an impressive 3x faster printing speed, effectively addressing the common problem of lengthy prints associated with other TPU filaments. TPU 95A HF maintains exceptional interlayer adhesion, impact resistance, flexibility, and cold-temperature resilience, just like traditional TPU filaments. Experience faster TPU printing without any compromises.

• Specifications

Subjects	Data
Diameter	1.75 mm
Net Filament Weight	1 kg
Spool Material	PC + ABS (Temperature resistance 90 °C)
Spool Size	Diameter: 200 mm; Height: 67 mm

• Recommended Printing Settings

Subjects	Data
Drying Settings before Printing	Blast Drying Oven: 70 °C, 8 h X1 Series Printer Heatbed: 80 - 90 °C, 12 h
Printing and Storage Humidity	< 20% RH (Sealed with desiccant)
Nozzle Size	0.4, 0.6, 0.8 mm
Nozzle Temperature	220 - 240 °C
Build Plate Type	Cool Plate, Engineering Plate, High Temperature Plate or Textured PEI Plate
Bed Surface Preparation	Glue
Bed Temperature	30 - 35 °C
Cooling Fan	Turn on
Printing Speed	< 200 mm/s
Retraction Length	0.8 - 1.4 mm
Retraction Speed	20 - 40 mm/s
Chamber Temperature	25 - 45 °C

Max Overhang Angle	~ 55°
Max Bridging Length	20 mm

• Properties

Bambu Lab has tested the differing aspects in the performance of TPU 95A HF material, including physical, mechanical, and chemical properties. Typical values are listed as followed:

Physical Properties		
Subjects	**Testing Methods**	**Data**
Density	ISO 1183	1.22 g/cm³
Melt Index	210 °C, 2.16 kg	36.5 ± 2.6 g/10 min
Melting Temperature	DSC, 10 °C/min	183 °C
Glass Transition Temperature	DSC, 10 °C/min	N / A
Crystallization Temperature	DSC, 10 °C/min	N / A
Vicar Softening Temperature	ISO 306, GB/T 1633	N / A
Heat Deflection Temperature	ISO 75 1.8 MPa	N / A
Heat Deflection Temperature	ISO 75 0.45 MPa	N / A
Saturated Water Absorption Rate	25 °C, 55% RH	1.08%

Mechanical Properties		
Subjects	**Testing Methods**	**Data**
Young's Modulus (X-Y)	ISO 527, GB/T 1040	9.8 ± 0.7 MPa
Young's Modulus (Z)	ISO 527, GB/T 1040	7.4 ± 0.6 MPa
Tensile Strength (X-Y)	ISO 527, GB/T 1040	27.3 ± 0.8 MPa
Tensile Strength (Z)	ISO 527, GB/T 1040	22.3 ± 0.6 MPa
Breaking Elongation Rate (X-Y)	ISO 527, GB/T 1040	> 650%
Breaking Elongation Rate (Z)	ISO 527, GB/T 1040	> 480%
Bending Modulus (X-Y)	ISO 178, GB/T 9341	N/A
Bending Modulus (Z)	ISO 178, GB/T 9341	N/A
Bending Strength (X-Y)	ISO 178, GB/T 9341	N/A
Bending Strength (Z)	ISO 178, GB/T 9341	N/A
Impact Strength (X-Y)	ISO 179, GB/T 1043	123.2 kJ/m²
Impact Strength (Z)	ISO 179, GB/T 1043	86.3 kJ/m²

Other Physical and Chemical Properties	
Subjects	**Data**
Odor	Odorless
Composition	Thermoplastic polyurethane
Skin Hazards	No hazard
Chemical Stability	Stable under normal storage and handling conditions
Solubility	Insoluble in water
Resistance to Acid	Not resistant
Resistance to Alkali	Not resistant
Resistance to Organic Solvent	Not resistant to some organic solvents
Resistance to Oil and Grease	Resistant to most kinds of oil and grease
Flammability	Flammable
Combustion Products	Water, carbon oxides, nitrogen oxides
Odor of Combustion Products	Pungent odor

- **Specimen Test**

Specimen Printing Conditions	
Subjects	**Data**
Nozzle Temperature	230 °C
Bed Temperature	35 °C
Printing Speed	140 mm/s
Infill Density	100%

**All the specimens were annealed and dried at 70 °C for 12 h before testing. It's not recommended to anneal prints of TPU, or prints with not very simple shape and structure can deform obviously. When drying the filament and annealing the prints, it's required to use an oven that has big enough inside volume and can provides even temperature distribution, such as a blast drying oven (forced-air drying oven), and the filament and prints need to be away from the heater, and a micro-wave oven or kitchen oven is not compatible, otherwise the filament and prints can get damaged.*

1. Tensile Testing

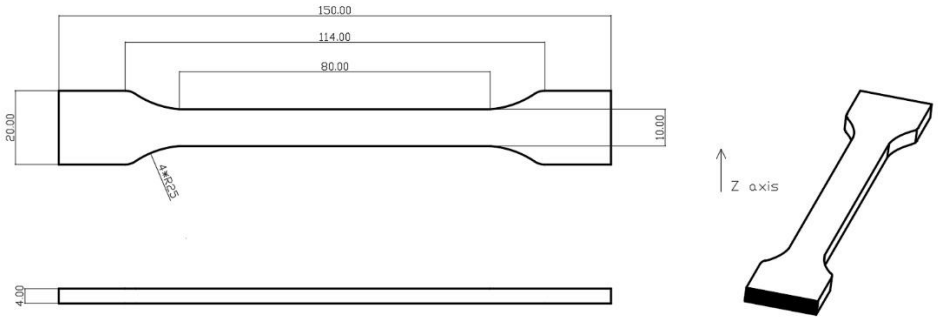

2. Bending Testing

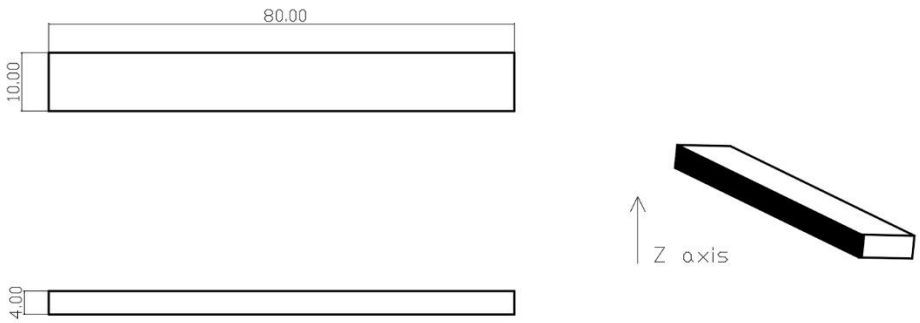

3. Impact Testing

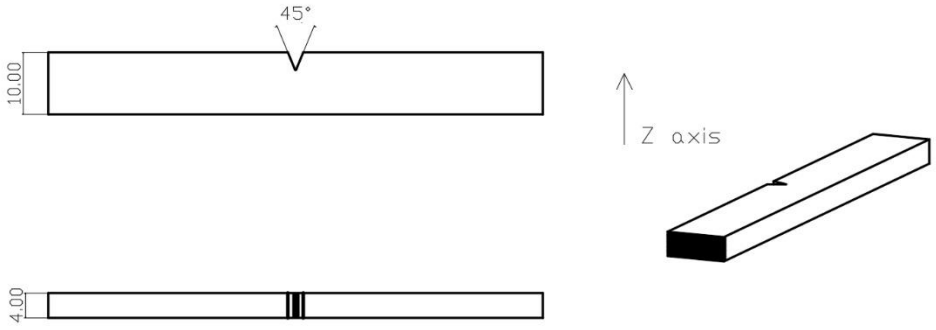

- **Disclaimer**

The performance values are tested by standard samples at Bambu Lab, and the values are for design reference and comparison only. Actual 3D printing model performance is related

to many other factors, including printers, printing conditions, printing models, printing parameters, etc.

In the process of using Bambu Lab 3D printing filaments, users are responsible for the legality, safety, and performance indicators of printing. Bambu Lab is not responsible for the use of materials and scenarios and is not responsible for any damage that occurs in the process of using our filaments.

Appendix D: Overview of fabricated samples

Name	Series	Straight or Curved	Flexure Angle	Flexure Thickness	Colour	Flexure Length	Flexure Stand Height	Flexure Stand Width	Base Height	Total Width	Total Height	
Sk_A10_T1.5	A	S	10	1.5	k	10	8	8	6	107.09	97.21	
Ck_A10_T1.5	A	C	10	1.5	k	10	8	8	6	107.09	97.21	
Sb_A18.75_T1.5	A2	S	18.75	1.5	b	10	8	8	6	104.82	101.64	
Cb_A18.75_T1.5	A2	C	18.75	1.5	b	10	8	8	6	104.82	101.64	
Sk_A27.5_T1.5	A	S	27.5	1.5	k	10	8	8	6	101.22	105.85	
Ck_A27.5_T1.5	A	C	27.5	1.5	k	10	8	8	6	101.22	105.85	
Sb_A36.25_T1.5	A2	S	36.25	1.5	b	10	8	8	6	96.39	109.74	
Cb_A36.25_T1.5	A2	C	36.25	1.5	b	10	8	8	6	96.39	109.74	
Sk_A45_T1.5	A	S	45	1.5	k	10	8	8	6	90.43	113.21	
Ck_A45_T1.5	A	C	45	1.5	k	10	8	8	6	90.43	113.21	
Sb_A53.75_T1.5	A2	S	53.75	1.5	b	10	8	8	6	83.48	116.19	
Cb_A53.75_T1.5	A2	C	53.75	1.5	b	10	8	8	6	83.48	116.19	
Sk_A62.5_T1.5	A	S	62.5	1.5	k	10	8	8	6	75.7	118.61	
Ck_A62.5_T1.5	A	C	62.5	1.5	k	10	8	8	6	75.7	118.61	
Sk_A80_T1.5	A	S	80	1.5	k	10	8	8	6	58.42	121.54	
Ck_A80_T1.5	A	C	80	1.5	k	10	8	8	6	58.42	121.54	
Sb_A27.5_T0.6	B	S	27.5	0.6	b	10	8	8	6	101.22	105.85	
Sb_A27.5_T0.9	B	S	27.5	0.9	b	10	8	8	6	101.22	105.85	
Sb_A27.5_T1.2	B	S	27.5	1.2	b	10	8	8	6	101.22	105.85	
Sb_A27.5_T1.8	B	S	27.5	1.8	b	10	8	8	6	101.22	105.85	
Sb_A27.5_T2.1	B	S	27.5	2.1	b	10	8	8	6	101.22	105.85	
Sb_A27.5_T2.4	B	S	27.5	2.4	b	10	8	8	6	101.22	105.85	
Sb_A10_T1.5	A3	S	10	1.5	b	10	8	8	6	107.09	97.21	
Cb_A10_T1.5	A3	C	10	1.5	b	10	8	8	6	107.09	97.21	
Sb_A27.5_T1.5	A3	S	27.5	1.5	b	10	8	8	6	101.22	105.85	
Cb_A27.5_T1.5	A3	C	27.5	1.5	b	10	8	8	6	101.22	105.85	
Sb_A45_T1.5	A3	S	45	1.5	b	10	8	8	6	90.43	113.21	
Cb_A45_T1.5	A3	C	45	1.5	b	10	8	8	6	90.43	113.21	
Sb_A62.5_T1.5	A3	S	62.5	1.5	b	10	8	8	6	75.7	118.61	
Cb_A62.5_T1.5	A3	C	62.5	1.5	b	10	8	8	6	75.7	118.61	

Appendix E: Code Snippet Dynamic Recording using Arduino

```
%% Live Angle Data Acquisition

a = arduino; % Use the arduino command to connect to an arduino device.
% Duration of the test in seconds
Test_length = 6;

figure
h = animatedline;
ax = gca;
ax.YGrid = 'on';
ax.YLim = [0 360];

% Initialize timer
startTime = datetime('now');
stop = false;

% Start live data acquisition loop
while ~stop
    % --- Read and convert analog voltage to angle ---
    v = readVoltage(a, 'A0');       % Read voltage from analog pin A0
    v_part = v/5 - 0.1;             % Normalize and apply offset
    angle_deg = 360 * (1 - abs(v_part / 0.8)); % Convert to angle in degrees

    % --- Get elapsed time in seconds ---
    t = datetime('now') - startTime;
    t_sec = seconds(t);

    % --- Plot current point on live chart ---
    addpoints(h, t_sec, angle_deg);
    drawnow limitrate; % Reduces CPU usage by limiting update rate

    % --- Stop condition ---
    if t_sec >= Test_length
        stop = true;
    end
end

[timeLogs, angleLogs] = getpoints(h); % Extract logged data
```

Appendix F: Code Snippet Tensile Data Analysis

```
%% Function to compute dissipated energy from tensile test data
% Returns dissipation values for single and repeated samples as a function of
    angle.
% For the use of sample series with variating Angle

function [dissipatedEnergy, Alist, dissipatedEnergy_single, Alist_single] =
    computeDissipatedEnergyAngle(straightOrCurved, colourTPU, inputAngle,
    thicknessFixed, repIndex, sampleRepetition)

    % Initialize outputs
    dissipatedEnergy = [];
    Alist = [];
    dissipatedEnergy_single = [];
    Alist_single = [];

    for i = 1:length(inputAngle)
        angleStr = num2str(inputAngle(i));

        %% --- Single Test File ---
        filenameSingle = sprintf('TensileTestdata_%s%s_A%s_T%s_%s.csv', ...
            straightOrCurved, colourTPU, angleStr, num2str(thicknessFixed),
                repIndex{1});

        if isfile(filenameSingle)
            data = readmatrix(filenameSingle, detectImportOptions(filenameSingle))
                ;

            % Split data in half to be used in the calculation of the
            % dissipated energy
            [~, maxIdx] = max(data(:, 2));
            firstHalf = data(1:maxIdx, :);
            secondHalf = flipud(data(maxIdx:end, :));

            areaFirst = trapz(firstHalf(:, 2), firstHalf(:, 3));
            areaSecond = trapz(secondHalf(:, 2), secondHalf(:, 3));
            lossRatio = (areaFirst - areaSecond) / areaFirst;

            if lossRatio > 0 && ~isnan(lossRatio)
                dissipatedEnergy_single(end+1) = lossRatio;
                Alist_single(end+1) = inputAngle(i);
            end
        else
            fprintf('File not found: %s. Skipping single test.\n', filenameSingle)
                ;
```

```
        end

        %% --- Repeated Test File ---
        filenameRepeat = sprintf('TensileTestdata_%s%s_A%s_T%s_%s.csv', ...
            straightOrCurved, colourTPU, angleStr, num2str(thicknessFixed),
                repIndex{2});

        if ~isfile(filenameRepeat)
            fprintf('File not found: %s. Skipping repeated test.\n',
                filenameRepeat);
            continue;
        end

        data = readmatrix(filenameRepeat, detectImportOptions(filenameRepeat));
        totalRows = size(data, 1);
        segmentLength = floor(totalRows / sampleRepetition);

        % Same as before, but this time the data has 5 repetitions and
        % needs to be split before splitting it in the five corresponding
        % dissipation data
        for j = 1:sampleRepetition
            idxStart = (j - 1) * segmentLength + 1;
            idxEnd = j * segmentLength;

            if j == sampleRepetition
                idxEnd = totalRows; % Ensure last segment includes all remaining
                    data
            end

            segment = data(idxStart:idxEnd, :);

            [~, maxIdx] = max(segment(:, 2));
            firstHalf = segment(1:maxIdx, :);
            secondHalf = flipud(segment(maxIdx:end, :));

            areaFirst = trapz(firstHalf(:, 2), firstHalf(:, 3));
            areaSecond = trapz(secondHalf(:, 2), secondHalf(:, 3));
            lossRatio = (areaFirst - areaSecond) / areaFirst;

            if lossRatio > 0 && ~isnan(lossRatio)
                dissipatedEnergy(end+1) = lossRatio;
                Alist(end+1) = inputAngle(i);
            end
        end
    end
end
```

Appendix G: Code Snippet Dynamic Data Analysis

```
%% Function to compute the dissipated energy from the Dynamic data
% Returns matrix of dissipation values for all combinations of the input
% angles and masses.
% For the use of samples with variating Angles

function [Alist_out, Mlist_out, dissipatedEnergy_out] = DissipatedEnergyAngle(
    straightOrCurved, colourTPU, inputAngle, thicknessFixed, inputMass,
    sampleRepetition)
    % Physical parameters of test setup
    armTotalMass = [1,1+0.535,1+1.044,1+1.550]; %[kg]
    armCenterMass = [0.254,0.340,0.380,0.404];  %[m]

    % Initialize outputs
    Datapoints = length(inputMass)*length(inputAngle)*sampleRepetition;
    Alist_out = zeros(Datapoints, 1);
    Mlist_out = zeros(Datapoints, 1);
    dissipatedEnergy_out = zeros(Datapoints, 1);

    for i = 1:length(inputMass)
        for j = 1:length(inputAngle)
            index = i+(j-1)*length(inputMass);

            for k = 1:sampleRepetition
                fullindex = k+(index-1)*sampleRepetition;
                Filename = sprintf('Testdata_%s%s_A%s_T%s_M%s_%d.csv', ...
                    straightOrCurved, colourTPU, num2str(inputAngle(j)), num2str(
                        thicknessFixed), num2str(inputMass(i)), k);
                if exist(Filename, 'file') == 0
                    %fprintf('File not found: %s. Skipping...\n', Filename);
                    continue;
                end

                opts = detectImportOptions(Filename);
                data = readmatrix(Filename, opts);

                % Smooth data to find minima without noise
                smoothedAngle = smooth(data(:,2),10);
                [peakValues, peakIndices] = findpeaks(-smoothedAngle);
                peakValues = -peakValues;

                if isempty(peakValues) || length(peakValues) < 2
                    continue;
                end

```

```
                firstValue = peakValues(1);
                idx = find(peakValues > 80, 1, 'first');

                if isempty(idx)
                    continue;
                end

                % Use the values of the first positiona and the first peak
                % to find the respective potential energies.
                firstPeak = data(peakIndices(idx), 2);
                potentialEnegryStart = armTotalMass(i)*(armCenterMass(i)+cosd(
                    firstValue)*armCenterMass(i));
                potentialEnegryFirstpeak = armTotalMass(i)*(armCenterMass(i)+cosd(
                    firstPeak)*armCenterMass(i));
                energyLost = potentialEnegryStart - potentialEnegryFirstpeak;

                dissipatedEnergy_out(fullindex) = energyLost /
                    potentialEnegryStart;
                Mlist_out(fullindex) = inputMass(i);
                Alist_out(fullindex) = inputAngle(j);
            end
        end
    end
end
```